

## Impact of uniaxial pressure on structural and magnetic phase transitions in electron-doped iron pnictides

Xingye Lu,<sup>1,2,\*</sup> Kuo-Feng Tseng,<sup>3,4</sup> T. Keller,<sup>3,4</sup> Wenliang Zhang,<sup>2</sup> Ding Hu,<sup>2</sup> Yu Song,<sup>1</sup> Haoran Man,<sup>1</sup> J. T. Park,<sup>5</sup> Huiqian Luo,<sup>2</sup> Shiliang Li,<sup>2,6</sup> Andriy H. Nevidomskyy,<sup>1</sup> and Pengcheng Dai<sup>1,†</sup>

<sup>1</sup>*Department of Physics and Astronomy & Rice Center for Quantum Materials, Rice University, Houston, Texas 77005, USA*

<sup>2</sup>*Beijing National Laboratory for Condensed Matter Physics, Institute of Physics, Chinese Academy of Sciences, Beijing 100190, China*

<sup>3</sup>*Max-Planck-Institut für Festkörperforschung, Heisenbergstrasse 1, D-70569 Stuttgart, Germany*

<sup>4</sup>*Max Planck Society Outstation at the Forschungsneutronenquelle Heinz Maier-Leibnitz (MLZ), D-85747 Garching, Germany*

<sup>5</sup>*Heinz Maier-Leibnitz Zentrum (MLZ), Technische Universität München, 85748 Garching, Germany*

<sup>6</sup>*Collaborative Innovation Center of Quantum Matter, Beijing, China*

(Received 15 July 2015; revised manuscript received 20 March 2016; published 28 April 2016)

We use neutron resonance spin echo and Larmor diffraction to study the effect of uniaxial pressure on the tetragonal-to-orthorhombic structural ( $T_s$ ) and antiferromagnetic (AF) phase transitions in iron pnictides  $\text{BaFe}_{2-x}\text{Ni}_x\text{As}_2$  ( $x = 0, 0.03, 0.12$ ),  $\text{SrFe}_{1.97}\text{Ni}_{0.03}\text{As}_2$ , and  $\text{BaFe}_2(\text{As}_{0.7}\text{P}_{0.3})_2$ . In antiferromagnetically ordered  $\text{BaFe}_{2-x}\text{Ni}_x\text{As}_2$  and  $\text{SrFe}_{1.97}\text{Ni}_{0.03}\text{As}_2$  with  $T_N$  and  $T_s$  ( $T_N \leq T_s$ ), a uniaxial pressure necessary to detwin the sample also increases  $T_N$ , smears out the structural transition, and induces an orthorhombic lattice distortion at all temperatures. By comparing temperature and doping dependence of the pressure induced lattice parameter changes with the elastoresistance and nematic susceptibility obtained from transport and ultrasonic measurements, we conclude that the in-plane resistivity anisotropy found in the paramagnetic state of electron underdoped iron pnictides depends sensitively on the nature of the magnetic phase transition and a strong coupling between the uniaxial pressure induced lattice distortion and electronic nematic susceptibility.

DOI: [10.1103/PhysRevB.93.134519](https://doi.org/10.1103/PhysRevB.93.134519)

### I. INTRODUCTION

The parent compounds of iron pnictide superconductors such as  $\text{BaFe}_2\text{As}_2$  and  $\text{SrFe}_2\text{As}_2$  exhibit a tetragonal-to-orthorhombic structural transition at  $T_s$  followed by development of collinear antiferromagnetic (AF) order along the  $a$  axis of the orthorhombic lattice below  $T_N$  [left inset in Fig. 1(a) and  $T_s \approx T_N$ ] [1–6]. Upon electron doping via partially substituting Fe by Co or Ni to form  $\text{BaFe}_{2-x}\text{TxAs}_2$  ( $T = \text{Co, Ni}$ ), the nearly coupled structural and magnetic phase transitions in  $\text{BaFe}_2\text{As}_2$  become two separate second order phase transitions at  $T_s$  and  $T_N$  ( $T_s > T_N$ ) that decrease in temperature with increasing  $x$  [7–10]. On the other hand, the coupled first-order structural and magnetic phase transitions in  $\text{SrFe}_2\text{As}_2$  [4], while decreasing in temperature with increasing  $x$  in  $\text{SrFe}_{2-x}\text{TxAs}_2$ , remain coupled first-order transitions leading up to superconductivity [11].

Because the structural and magnetic phase transitions in  $\text{BaFe}_{2-x}\text{TxAs}_2$  and  $\text{SrFe}_{2-x}\text{TxAs}_2$  occur below room temperature, iron pnictides in the orthorhombic AF ground state will form twin domains with AF Bragg peaks appearing at the in-plane  $(\pm 1, 0)$  and  $(0, \pm 1)$  positions in reciprocal space [right inset in Fig. 1(a)] [6]. To probe the intrinsic electronic properties of these materials, one can apply uniaxial pressure along one axis of the orthorhombic lattice to obtain single domain samples [12–15]. Indeed, transport measurements on uniaxial pressure detwinned electron-doped  $\text{BaFe}_{2-x}\text{TxAs}_2$  ( $T = \text{Co, Ni}$ ) reveal in-plane resistivity anisotropy in the AF state that persists to temperatures above the zero-pressure

$T_N$  and  $T_s$  [12–15]. On the other hand, similar transport measurements on uniaxial pressure detwinned  $\text{SrFe}_{2-x}\text{TxAs}_2$  ( $T = \text{Co, Ni}$ ) indicate vanishingly small resistivity anisotropy at temperatures above the zero pressure coupled  $T_N$  and  $T_s$  [16–18]. Figure 1(b) compares temperature dependence of the resistivity anisotropy [defined as  $\Delta\rho = (\rho_b - \rho_a)/(\rho_b + \rho_a)$ , where  $\rho_a$  and  $\rho_b$  are resistivity along the  $a$  and  $b$  axis of the orthorhombic lattice, respectively] obtained under  $\sim 20$  MPa uniaxial pressure for  $\text{BaFe}_2\text{As}_2$ ,  $\text{BaFe}_{1.97}\text{Ni}_{0.03}\text{As}_2$ ,  $\text{SrFe}_{1.97}\text{Ni}_{0.03}\text{As}_2$ , and  $\text{SrFe}_2\text{As}_2$ . Consistent with earlier works [12–18], we find that resistivity anisotropy is much larger in  $\text{BaFe}_2\text{As}_2$  and  $\text{BaFe}_{1.97}\text{Ni}_{0.03}\text{As}_2$  at temperatures above  $T_N$ .

Although resistivity anisotropy in the paramagnetic state of the iron pnictides under applied uniaxial pressure suggests the presence of an electronic nematic phase that breaks the in-plane fourfold rotational symmetry ( $C_4$ ) of the underlying tetragonal lattice [19–24], much is unclear about the microscopic origin of the in-plane resistivity anisotropy and electronic nematic phase [25–38]. Since neutron-scattering experiments reveal that uniaxial pressure necessary to detwin the sample also increases  $T_N$  of the system, the observed in-plane resistivity anisotropy above the zero pressure  $T_N$  and  $T_s$  may arise from the increased  $T_N$  and intrinsic anisotropic nature of the collinear AF phase [39,40]. Furthermore, while it is generally assumed that the uniaxial pressure for sample detwinning has negligible effect on the lattice parameters of the iron pnictides [12–15], the precise effect of uniaxial pressure on structural distortion of these materials is unknown. From neutron extinction effect measurements, a uniaxial pressure is suggested to push structural fluctuations related to the orthorhombic distortion to a temperature well above the zero-pressure value of  $T_s$  [41], similar to the effect on the resistivity anisotropy [12–15]. To understand

\*Present Address: Paul Scherrer Institut, Swiss Light Source, CH-5232 Villigen PSI, Switzerland.

†pdai@rice.edu

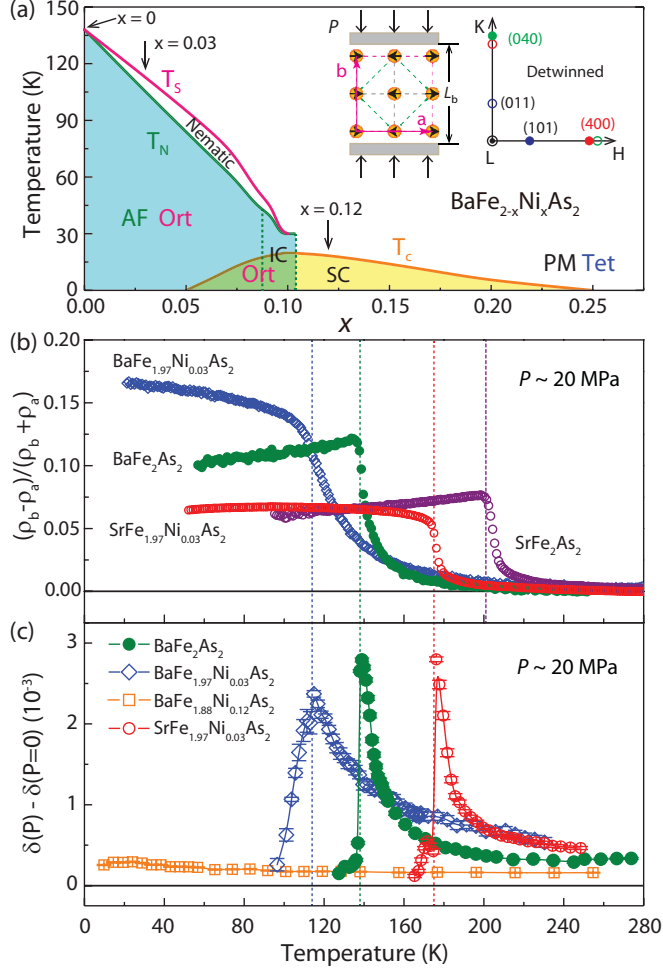


FIG. 1. (a) The schematic electronic phase diagram of  $\text{BaFe}_{2-x}\text{Ni}_x\text{As}_2$  with arrows marking  $x = 0, 0.03$ , and  $0.12$  samples described in the present study. The AF, PM, Ort, Tet, IC, SC are antiferromagnetic, paramagnetic, orthorhombic, tetragonal, incommensurate, and superconducting states, respectively [10]. The left inset shows the direction of the applied uniaxial pressure (marked by the vertical arrows) and the spin arrangements of Fe in the AF ordered iron pnictides, where  $a$  and  $b$  are the orthorhombic axes. The right inset shows the corresponding reciprocal lattice. All the marked positions have AF or nuclear Bragg peaks for a twinned sample, while the positions marked by open symbols have vanishing scattering intensity for a detwinned sample. (b) Temperature dependence of the resistivity anisotropy for  $\text{BaFe}_{2-x}\text{Ni}_x\text{As}_2$  and  $\text{SrFe}_{2-x}\text{Ni}_x\text{As}_2$  ( $x = 0, 0.03$ ) under  $P \approx 20$  MPa. (c) Summary of temperature dependence of the uniaxial pressure induced lattice distortion at  $P \approx 20$  MPa [ $\delta(P \approx 20 \text{ MPa}) - \delta(P = 0 \text{ MPa})$ ] for  $\text{BaFe}_{2-x}\text{Ni}_x\text{As}_2$  ( $x = 0, 0.03, 0.12$ ) and  $\text{SrFe}_{1.97}\text{Ni}_{0.03}\text{As}_2$ . The actual data for  $x = 0.03, 0.12$  are normalized to 20 MPa assuming a linear relationship between uniaxial pressure and  $\delta$ . Uniaxial pressure induced lattice distortion vanishes rapidly below  $T_N$  marked by the vertical dashed lines in (b) and (c).

the microscopic origin of the in-plane resistivity anisotropy in the paramagnetic state [12–15], it is important to establish the effect of a uniaxial pressure on the magnetic and structural phase transitions of  $\text{BaFe}_{2-x}\text{Ni}_x\text{As}_2$  and  $\text{SrFe}_{2-x}\text{Ni}_x\text{As}_2$ , and determine if the electronic anisotropy in the paramagnetic

tetragonal phase of iron pnictides is intrinsic [42,43], or entirely due to the symmetry breaking uniaxial pressure applied to the materials [44,45]. It is also important to deduce what role the nature of the AF transition plays in the nematic susceptibility [17,25,26,38] and how the latter depends on the uniaxial pressure.

In this article, we use neutron resonance spin echo (NRSE) [46,47] and Larmor diffraction [48] to study the effect of uniaxial pressure on the structural and magnetic phase transitions in electron-doped iron pnictides  $\text{BaFe}_{2-x}\text{Ni}_x\text{As}_2$  with  $x = 0, 0.03, 0.12$  [9,10] and  $\text{SrFe}_{1.97}\text{Ni}_{0.03}\text{As}_2$  [18], and in the isovalently doped  $\text{BaFe}_2(\text{As}_{0.7}\text{P}_{0.3})_2$  [49]. While the underdoped  $\text{BaFe}_{1.97}\text{Ni}_{0.03}\text{As}_2$  ( $T_N = 109$  K and  $T_S = 114$  K) exhibits a second-order AF transition below  $T_S$ ,  $\text{SrFe}_{1.97}\text{Ni}_{0.03}\text{As}_2$  has coupled first-order structural and magnetic phase transitions at  $T_N = T_S \approx 175$  K [50]. The electron overdoped  $\text{BaFe}_{1.88}\text{Ni}_{0.12}\text{As}_2$  ( $T_C = 18.6$  K) and isovalently doped  $\text{BaFe}_2(\text{As}_{0.7}\text{P}_{0.3})_2$  ( $T_C = 30$  K) have a paramagnetic tetragonal structure at all temperatures without static AF order. Figure 1(c) summarizes the key experimental result of the present work, where the temperature dependencies of the uniaxial pressure induced orthorhombic lattice distortions  $\delta(P \approx 20 \text{ MPa}) - \delta(P = 0 \text{ MPa})$  are determined using neutron Larmor diffraction for  $\text{BaFe}_2\text{As}_2$ ,  $\text{BaFe}_{1.97}\text{Ni}_{0.03}\text{As}_2$ ,  $\text{SrFe}_{1.97}\text{Ni}_{0.03}\text{As}_2$ , and  $\text{BaFe}_{1.88}\text{Ni}_{0.12}\text{As}_2$  [we defined the lattice distortion  $\delta = (a - b)/(a + b)$  with  $a$  and  $b$  being the orthorhombic lattice parameters]. Remarkably, the magnitude of our determined structural nematic susceptibility  $d\delta/dP \propto \delta(P) - \delta(0)$  in Fig. 1(c) is comparable in all three materials that have a structural phase transition, unlike the very different values of the resistivity anisotropy displayed in Fig. 1(b). Comparing these results with those of the elastoresistance and nematic susceptibility obtained from transport [20,23,24] and from elastic shear modulus/ultrasound spectroscopy measurements [38,51,52], we conclude that the resistivity anisotropy in the paramagnetic phase of the iron pnictides depends sensitively on whether the underlying magnetic phase transition is first or second order. We also find a strong coupling between the uniaxial pressure induced lattice distortion and the electronic nematic susceptibility, and have to be cautious in directly relating resistivity anisotropy to the nematic order parameter in the iron pnictides.

## II. RESULTS

### A. Experimental results

Our experiments were carried out using conventional thermal triple-axis spectrometer PUMA and three axes spin-echo spectrometer (TRISP) at the Forschungsneutronenquelle Heinz Maier-Leibnitz (MLZ), Garching, Germany. The principles of NRSE and Larmor diffraction are described elsewhere [50]. Single crystals of  $\text{BaFe}_{2-x}\text{Ni}_x\text{As}_2$ ,  $\text{SrFe}_{2-x}\text{Ni}_x\text{As}_2$ , and  $\text{BaFe}_2(\text{As}_{0.7}\text{P}_{0.3})_2$  were grown by self-flux method as described before [49,53]. We define the momentum transfer  $\mathbf{Q}$  in the three-dimensional reciprocal space in  $\text{\AA}^{-1}$  as  $\mathbf{Q} = H\mathbf{a}^* + K\mathbf{b}^* + L\mathbf{c}^*$ , where  $H$ ,  $K$ , and  $L$  are Miller indices and  $\mathbf{a}^* = \hat{\mathbf{a}}2\pi/a$ ,  $\mathbf{b}^* = \hat{\mathbf{b}}2\pi/b$ ,  $\mathbf{c}^* = \hat{\mathbf{c}}2\pi/c$  with  $a \approx b \approx 5.6$   $\text{\AA}$ , and  $c = 12.96$   $\text{\AA}$  for  $\text{BaFe}_{2-x}\text{Ni}_x\text{As}_2$ . In this notation, the AF Bragg peaks should occur at  $(\pm 1, 0, L)$  ( $L = 1, 3, 5, \dots$ )

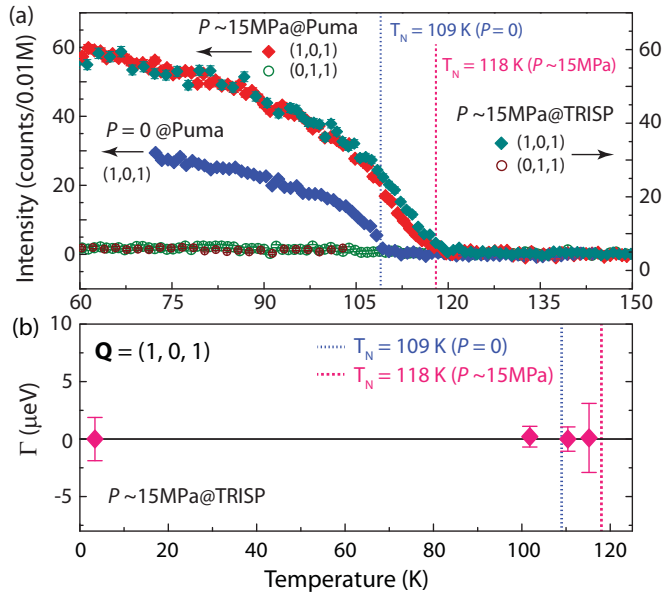


FIG. 2. (a) Magnetic order parameters at  $\mathbf{Q} = (1,0,1)$  for the zero ( $P = 0$ ) and uniaxial pressured ( $P \sim 15$  MPa)  $\text{BaFe}_{1.97}\text{Ni}_{0.03}\text{As}_2$ .  $T_N$  is 109 K for an unpressured sample (blue diamonds). Upon applying uniaxial pressure of  $P \approx 15$  MPa, the  $T_N$  is enhanced to 118 K and the sample becomes 100% detwinned as seen by PUMA and TRISP measurements. (b) The energy linewidth (half width at half maximum,  $\Gamma$ ) of the magnetic Bragg peak  $\mathbf{Q} = (1,0,1)$  measured by NRSE using TRISP for  $\text{BaFe}_{1.97}\text{Ni}_{0.03}\text{As}_2$ . The blue and red dashed lines indicate  $T_N$  in  $P = 0$  and 15 MPa uniaxial pressure, respectively. The slight larger errors of  $\Gamma$  near  $T_N$  is due to low statistics data.

positions in reciprocal space of a completely detwinned sample [right inset in Fig. 1(a)]. For neutron-scattering experiments, single crystals are aligned in either the  $[H, K, H + K]$  [41] or  $[H, K, 0]$  zone.

We first discuss the effect of uniaxial pressure on the collinear AF order in  $\text{BaFe}_{2-x}\text{TxAs}_2$ . In previous neutron-scattering work on  $\text{BaFe}_{2-x}\text{Co}_x\text{As}_2$ , the Néel temperature ( $T_N$ ) was found to be pushed to higher temperature under uniaxial strain field, forming a broader magnetic transition [39,40]. Moreover, it seems that the increase in  $T_N$  depends on the annealing condition [41,54]. Although the  $T_N$  enhancement was attributed to uniaxial strain aligned fluctuating magnetic domains, the effect of uniaxial pressure on the ordered moment remains elusive and the nature of the  $T_N$  enhancement is still under debate [40,41,54].

By aligning single crystals in the  $[1,0,1] \times [0,1,1]$  scattering plane [41], we were able to determine  $T_N$ , detwinning ratio, as well as the ordered moment of the system under zero and finite uniaxial pressures. Figure 2(a) shows temperature dependence of the  $(1,0,1)$  and  $(0,1,1)$  magnetic scattering intensity for  $\text{BaFe}_{1.97}\text{Ni}_{0.03}\text{As}_2$  obtained using PUMA [left axis in Fig. 2(a)] and TRISP (right axis). The two sets of data are in excellent quantitative agreement with each other. Under the applied uniaxial pressure of  $P \approx 15$  MPa, the Néel temperature increases from  $T_N \approx 109$  K (at  $P = 0$ ) to  $T_N \approx 118$  K. The magnetic scattering intensity [Fig. 2(a)] in the  $(1,0,1)$  peak becomes approximately twice as large as in the twinned sample, whereas the  $(0,1,1)$  peak vanishes,

suggesting that the sample is completely detwinned and the applied uniaxial pressure does not significantly affect the ordered moment.

To test whether the  $T_N$  increase is an intrinsic feature of the system, we note that the magnetic order parameter under uniaxial pressure has a round tail around  $T_N$  [39,40], suggesting that the  $T_N$  enhancement could arise from enhanced slow spin dynamics (critical scattering) under inhomogeneous uniaxial strain field and cannot be resolved by conventional triple-axis neutron diffraction due to its coarse energy resolution ( $\Delta E \approx 0.3\text{--}1$  meV). To clarify the nature of the increase in  $T_N$ , we have measured the energy linewidth [ $\Gamma \geq 0$ ; see Fig. 2(b)] of the quasielastic scattering for magnetic reflection  $(1,0,1)$  using high-energy resolution ( $\Delta E \approx 1$   $\mu\text{eV}$ ) NRSE at TRISP [55]. As seen in Fig. 2(b), the  $\Gamma$  at all measured temperatures are resolution limited, indicating that the increase in magnetic scattering intensity below  $T_N \approx 118$  K is elastic ( $\Gamma \leq 1$   $\mu\text{eV}$ ), and an intrinsic nature of the system.

To determine the effect of uniaxial pressure on the tetragonal-to-orthorhombic phase transition in iron pnictides, we carried out neutron Larmor diffraction experiments capable of measuring minor change of lattice spacing  $d = 2\pi/|\mathbf{Q}(H, K, L)|$  and its spread  $\Delta d$  with a resolution better than  $10^{-5}$  in  $\Delta d/d$  [inset in Fig. 3(a)] [48,50]. We focus on  $(4,0,0)$  and  $(0,4,0)$  nuclear Bragg reflections corresponding to a  $d$  spacing  $d \approx a/4$ , which we measured in  $\text{BaFe}_{2-x}\text{Ni}_x\text{As}_2$  ( $x = 0, 0.03, 0.12$ ),  $\text{SrFe}_{1.97}\text{Ni}_{0.03}\text{As}_2$ , and  $\text{BaFe}_2(\text{As}_{0.7}\text{P}_{0.3})_2$  both on freshly prepared samples (uniaxial pressure  $P = 0$ ) and under uniaxial pressure ( $P \approx 10, 20$  MPa). Figure 3 shows the temperature and pressure dependence of the  $d$  spread for these samples. The  $d$  spread is characterized by the FWHM (full width at half maximum) of the lattice spacing distribution  $f(\Delta d/d)$ , which is assumed to be a Gaussian distribution [50]. The diamonds in Fig. 3(a) show temperature dependence of the FWHM for  $\text{BaFe}_2\text{As}_2$  at zero pressure. Similar to  $\text{BaFe}_{1.97}\text{Ni}_{0.03}\text{As}_2$  [45], temperature dependence of FWHM follows a Curie-Wiess form and peaks around the zero-pressure value of  $T_N \approx T_s$ . Upon application of a uniaxial pressure  $P \approx 20$  MPa, the magnitude of FWHM increases at all temperatures and now peaks at an enhanced  $T_N = 144$  K [Fig. 3(a)].

Figure 3(b) shows similar data for  $\text{SrFe}_{1.97}\text{Ni}_{0.03}\text{As}_2$ , where there are coupled strong first-order structural and AF phase transitions at  $T_N = T_s = 175$  K [11]. Compared with  $\text{BaFe}_2\text{As}_2$ , where the AF phase transition is weakly first order and structural transition is second order [5], the AF and structural transition induced changes in FWHM are much smaller and confined to temperatures close to  $T_N \approx T_s$  in  $\text{SrFe}_{1.97}\text{Ni}_{0.03}\text{As}_2$  [Fig. 3(b)]. Under a uniaxial pressure  $P \approx 20$  MPa, however, both the FWHM and  $T_N$  increase dramatically with solid lines showing Curie-Wiess fits to the data. For  $\text{BaFe}_{1.97}\text{Ni}_{0.03}\text{As}_2$ , application of a  $P \approx 10$  MPa uniaxial pressure transforms temperature dependence of the FWHM, which forms a broad peak above the zero-pressure value of  $T_s$ . Upon releasing the uniaxial pressure [ $P$  released, filled green diamonds in Fig. 3(c)], the system goes back to the original unpressured fresh state.

Figure 3(d) compares temperature dependence of the FWHM for electron overdoped  $\text{BaFe}_{1.88}\text{Ni}_{0.12}\text{As}_2$  and  $\text{BaFe}_2(\text{As}_{0.7}\text{P}_{0.3})_2$ , where both materials are in the param-

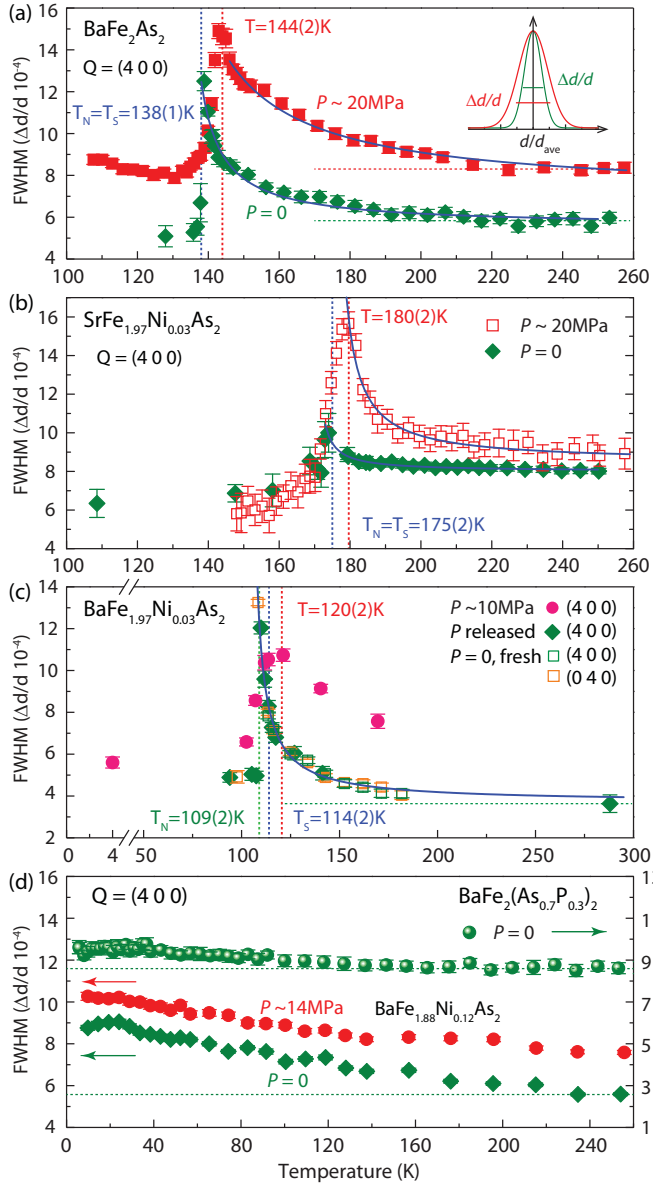


FIG. 3. Temperature dependence of full width at half maximum (FWHM) of  $\Delta d/d$  in several iron pnictides under different uniaxial pressures obtained from neutron Larmor diffraction experiments [50]. (a) Temperature dependence of  $\Delta d/d$  in FWHM for the (4,0,0) Bragg reflection of  $\text{BaFe}_2\text{As}_2$  at  $P = 0$  and 20 MPa. The solid line above  $T_N$  is a fit using Curie-Weiss formalism [ $\text{FWHM}(T) = A/(T - T_1) + B$ , where  $A$ ,  $B$ , and  $T_1$  are fitting parameters]. (b) Similar data for  $\text{SrFe}_{1.97}\text{Ni}_{0.03}\text{As}_2$ . The vertical blue and red dashed lines in (a) and (b) mark the  $T_N$  of the sample at zero and finite pressure, respectively. (c) Similar data for  $\text{BaFe}_{1.97}\text{Ni}_{0.03}\text{As}_2$ , where the vertical green and blue dashed lines mark  $T_N$  and  $T_s$ , respectively, at zero pressure. The open green and yellow squares mark measurements of FWHM under zero pressure (fresh) at the (4,0,0) and (0,4,0) Bragg peaks, respectively. The pink solid circles are identical measurements under  $P \approx 10$  MPa uniaxial pressure on (4,0,0). The solid green diamonds are data after uniaxial pressure is released. The vertical red dashed line indicates the peak position of the FWHM under  $P = 10$  MPa. (d) Temperature dependence of FWHM in  $\Delta d/d$  for  $\text{BaFe}_2(\text{As}_{0.7}\text{P}_{0.3})_2$  at  $P = 0$  MPa (solid green circles),  $\text{BaFe}_{1.88}\text{Ni}_{0.12}\text{As}_2$  at  $P = 0$  (solid green diamonds), and 14 MPa (solid red circles).

agnetic tetragonal state without static AF order. The weak temperature dependence of FWHM in these materials suggests that the large temperature dependence of FWHM in AF ordered  $\text{BaFe}_{2-x}\text{Ni}_x\text{As}_2$  ( $x = 0, 0.03$ ) and  $\text{SrFe}_{1.97}\text{Ni}_{0.03}\text{As}_2$  is due to a strong magnetoelastic coupling. Although application of a  $P \approx 14$  MPa uniaxial pressure on  $\text{BaFe}_{1.88}\text{Ni}_{0.12}\text{As}_2$  increases the absolute value of FWHM, it is still weakly temperature dependent [Fig. 3(d)].

To further demonstrate the impact of uniaxial pressure on the tetragonal-to-orthorhombic structural transition in  $\text{BaFe}_{2-x}\text{Ni}_x\text{As}_2$  ( $x = 0, 0.03, 0.12$ ) and  $\text{SrFe}_{1.97}\text{Ni}_{0.03}\text{As}_2$ , we compare in Fig. 4 temperature dependence of the lattice parameters along the orthorhombic  $a$  and  $b$  axis directions under zero and finite uniaxial pressure. We first discuss results for  $\text{BaFe}_{2-x}\text{Ni}_x\text{As}_2$  with  $x = 0$  [Figs. 4(a) and 4(b)] and 0.03 [Figs. 4(c) and 4(d)]. At  $P = 0$ , the lattice parameters have  $a = b$  at temperatures above  $T_s$  (tetragonal phase) and decrease linearly with decreasing temperature [open diamonds and hexagons in Figs. 4(a) and 4(c)]. Upon application of a uniaxial pressure, the system becomes orthorhombic at all temperatures and the orthorhombic structural transition becomes a crossover [filled diamonds and hexagons in Figs. 4(a) and 4(c)]. Figures 4(b) and 4(d) show temperature dependence of the lattice orthorhombicity  $\delta = (a - b)/(a + b)$  at different uniaxial pressures for  $x = 0$ , and 0.03, respectively. For unpressured fresh samples ( $P = 0$ ), and after the pressure has been released, the tetragonal structure becomes orthorhombic below  $T_s$  and the AF order below  $T_N$  further enhances the lattice orthorhombicity [5]. Upon applying the uniaxial pressure  $P \approx 10, 15$ , and 20 MPa, the temperature dependence of the lattice orthorhombicity becomes remarkably similar to that of the  $B_{2g}$  elastoresistance and nematic susceptibility of  $\text{BaFe}_{2-x}\text{Ni}_x\text{As}_2$  obtained from transport [23,24] and elastic shear modulus/ultrasound spectroscopy measurements [38,51,52], respectively.

## B. Theoretical Ginzburg-Landau analysis

To understand the temperature dependence of the pressure-induced lattice orthorhombicity described in Figs. 4(b) and 4(d), we consider the Ginzburg-Landau free-energy formalism used in previous works [20,38]:

$$F[\varphi, \delta] = F_0 + \frac{a}{2}(T - T_0)\varphi^2 + \frac{\tilde{B}}{4}\varphi^4 + \frac{C_{66,0}}{2}\delta^2 - \lambda\delta\varphi - P\delta, \quad (1)$$

where the electronic nematic order parameter  $\varphi$  is coupled linearly to the orthorhombic lattice distortion  $\delta$ . It then follows that (see the Appendix [50])

$$\delta = (\lambda(\varphi) + P)/C_{66,0}, \quad (2)$$

where  $C_{66,0}$  is the bare elastic constant that has no strong temperature dependence and  $P$  is the conjugate uniaxial pressure (stress) [38,41,50–52]. In the absence of the elasto-nematic coupling ( $\lambda = 0$ ), the nematic susceptibility  $\chi_\varphi = 1/[a(T - T_0)]$  is characterized by the Curie-Weiss temperature  $T_0$ . Upon considering the coupling between the nematic order parameter  $\varphi$  and the structural lattice distortion  $\delta$  (or equivalently, the elastic shear strain  $\varepsilon_6$ ), the elastic susceptibility takes on the

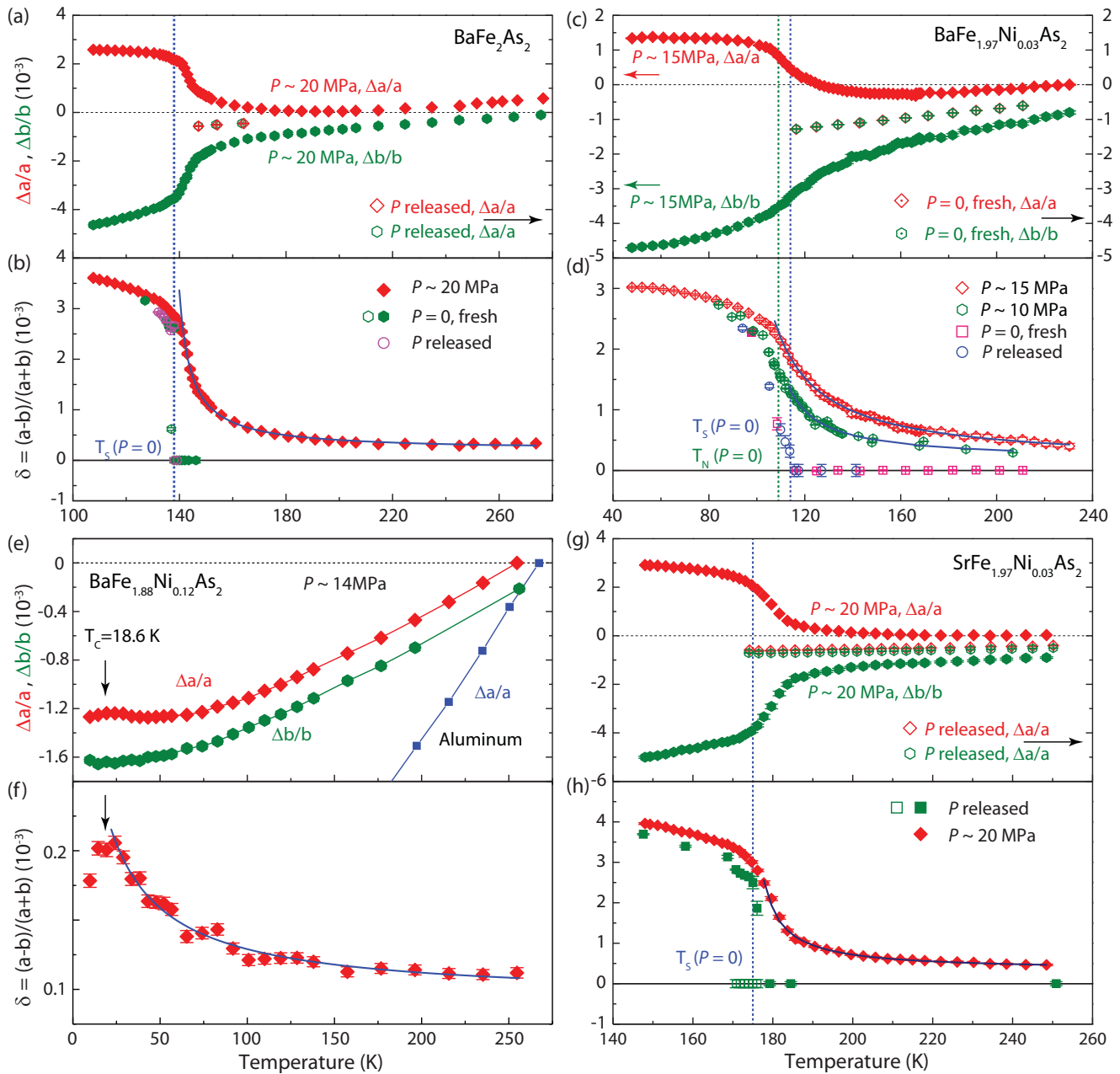


FIG. 4. Temperature dependence of the  $a$  and  $b$  lattice parameters and orthorhombicity  $\delta$  under different uniaxial pressure conditions ( $P = 0$  fresh,  $\sim 10$ ,  $\sim 15$ ,  $\sim 20$ , and  $0$  released MPa) for  $\text{BaFe}_{2-x}\text{Ni}_x\text{As}_2$  ( $x = 0, 0.03, 0.12$ ) and  $\text{SrFe}_{1.97}\text{Ni}_{0.03}\text{As}_2$ . (a) Temperature dependence of the  $a$  and  $b$  under  $P = 0$  and  $20$  MPa uniaxial pressure for  $\text{BaFe}_2\text{As}_2$ . (b) Temperature dependence of  $\delta$  under different uniaxial pressure ( $P = 0$  fresh,  $\sim 20$ , and  $0$  released MPa). The vertical blue dashed line marks the  $T_N/T_s$ . (c) Temperature dependence of the lattice parameters  $a$  and  $b$  at  $P = 0$  and  $15$  MPa for  $\text{BaFe}_{1.97}\text{Ni}_{0.03}\text{As}_2$ . (d) Temperature dependence of  $\delta$  under different uniaxial pressure ( $P = 0$  fresh,  $\sim 10$ ,  $\sim 15$ , and  $0$  released MPa). The open red diamonds and green hexagons are obtained by lattice thermal expansion measurements under uniaxial pressure. The pink squares are measurements of an unpressured fresh sample, while blue circles are obtained after releasing  $P \approx 10$  MPa uniaxial pressure. The blue circles and two pink squares below  $T_s$  are from zero pressure Larmor diffraction measurements. The pink squares above  $T_s$  are obtained from thermal-expansion measurements. The vertical green and blue dashed lines in (c) and (d) mark the  $T_N$  and  $T_s$  of the sample at zero pressure, respectively. (e) Temperature dependence of the  $a$  and  $b$  for  $\text{BaFe}_{1.88}\text{Ni}_{0.12}\text{As}_2$ . The lattice thermal expansion of aluminum is plotted as a reference [56]. The vertical arrow marks  $T_c = 18.6$  K and the solid lines are guides to the eye. (f) Temperature dependence of the orthorhombic lattice distortions calculated from (c). (g) Temperature dependence of the  $a$  and  $b$  lattice parameters for  $\text{SrFe}_{1.97}\text{Ni}_{0.03}\text{As}_2$  under  $P = 0$  fresh,  $20$ , and  $0$  (released) MPa. (h) Temperature dependence of  $\delta$  for the same pressure condition. The solid curves in (b), (d), (f), and (h) are fits using a Curie-Weiss functional form [50].

form [20,38]

$$\frac{d\delta}{dP} = \frac{1}{C_{66,0}} \frac{T - T_0}{T - T_s^{CW}} \quad (3)$$

with the renormalized nematic transition temperature  $T_s^{CW} = T_0 + \lambda^2/(aC_{66,0})$  that is increased compared to the bare Curie-Weiss temperature  $T_0$ . The pressure-induced lattice distortions in Figs. 4(b) and 4(d) can be well described by the Curie-Weiss functional form [50]. Therefore, uniaxial pressure induced orthorhombic lattice distortion and its temperature dependence in undoped and underdoped  $\text{BaFe}_{2-x}\text{Ni}_x\text{As}_2$  are directly associated with the nematic susceptibility [24,38]. Since the external uniaxial pressure explicitly breaks the tetragonal lattice symmetry, it turns the nematic transition at  $T_s = T_s^{CW}$  into a crossover, as is clearly seen in Fig. 4.

If the in-plane resistivity anisotropy in electron underdoped iron pnictides indeed arises from the coupling of the uniaxial-pressure induced lattice distortion  $\delta$  with the nematic susceptibility, it would be interesting to determine the effect of similar uniaxial pressure on the electron overdoped sample, where the resistivity anisotropy is known to be much weaker [14]. Figures 4(e) and 4(f) summarize the outcome of the neutron Larmor diffraction experiments on uniaxial pressured  $\text{BaFe}_{1.88}\text{Ni}_{0.12}\text{As}_2$ , which is tetragonal ( $a = b$ ) and nonmagnetic at all temperatures in zero pressure [10]. Figure 4(e) shows temperature dependence of the lattice parameter changes along the  $a$  axis ( $\Delta a/a$ ) and  $b$  axis ( $\Delta b/b$ ) under a uniaxial pressure of  $P \approx 14$  MPa. For comparison, the thermal contraction of aluminum is also shown [56]. Figure 4(f) shows the temperature dependence of the orthorhombic lattice distortion  $\delta$ , which reveals a clear anomaly at  $T_c$  consistent with ultrasonic spectroscopy measurements [51,52]. While the applied uniaxial pressure induces orthorhombic lattice distortion at 230 K, the magnitude of the lattice distortion,  $\delta \approx 1.1 \times 10^{-4}$ , is about five times smaller than that of  $\text{BaFe}_2\text{As}_2$  and  $\text{BaFe}_{1.97}\text{Ni}_{0.03}\text{As}_2$  at 230 K. On cooling to 20 K,  $\delta$  in  $\text{BaFe}_{1.88}\text{Ni}_{0.12}\text{As}_2$  increases to  $\sim 2 \times 10^{-4}$ , while  $\delta$  in  $\text{BaFe}_2\text{As}_2$  and  $\text{BaFe}_{1.97}\text{Ni}_{0.03}\text{As}_2$  becomes  $\sim 2.5 \times 10^{-3}$  near  $T_s$  [Figs. 4(b) and 4(d)], an order of magnitude larger than that of the electron overdoped compound.

To understand how a uniaxial pressure affects the first-order nature of the structural and magnetic phase transitions in  $\text{SrFe}_{1.97}\text{Ni}_{0.03}\text{As}_2$ , we compare in Figs. 4(g) and 4(h) temperature dependence of the lattice parameters and orthorhombicity under the zero and finite uniaxial pressure. At zero pressure, the first-order nature of the structural transition is clearly seen in hysteresis of temperature dependence of the lattice parameters and distortion [Figs. 4(g) and 4(h)]. Upon application of  $P \approx 20$  MPa uniaxial pressure, the lattice orthorhombicity no longer displays the first-order transition at  $T_s$ , but instead becomes a crossover, similar to that observed in the undoped and underdoped  $\text{BaFe}_{2-x}\text{Ni}_x\text{As}_2$  [see Figs. 4(b) and 4(d)].

Assuming that the application of the modest uniaxial pressure  $P \approx 20$  MPa can be considered in the linear-response regime [45], we can estimate the elastic susceptibility from the finite difference  $d\delta/dP \propto \Delta(\delta) = \delta(P \approx 20 \text{ MPa}) - \delta(P = 0)$  and compare it among the different compounds in the iron pnictide family. Figure 1(c) compares temperature dependence of  $\delta(P \approx 20 \text{ MPa}) - \delta(P = 0)$  for  $\text{BaFe}_{2-x}\text{Ni}_x\text{As}_2$

( $x = 0, 0.03, 0.12$ ) and  $\text{SrFe}_{1.97}\text{Ni}_{0.03}\text{As}_2$  normalized for  $P \approx 20$  MPa. For AF ordered  $\text{BaFe}_{2-x}\text{Ni}_x\text{As}_2$  ( $x = 0, 0.03$ ) and  $\text{SrFe}_{1.97}\text{Ni}_{0.03}\text{As}_2$ , the magnitudes of the pressure-induced lattice orthorhombicity are similar in the paramagnetic phase and vanish rapidly upon entering into the AF ordered state. Furthermore, the  $\delta(P \approx 20 \text{ MPa}) - \delta(P = 0)$  decreases for the iron pnictides with reduced  $T_N$ , and are much smaller for  $\text{BaFe}_{1.88}\text{Ni}_{0.12}\text{As}_2$ .

### III. DISCUSSION

It is well known that the effect of increasing electron doping in  $\text{BaFe}_{2-x}\text{Ni}_x\text{As}_2$  is to suppress the static AF order and to eliminate the low-temperature lattice orthorhombicity [7–10]. At zero pressure,  $\text{BaFe}_2\text{As}_2$  first exhibits a second-order structural transition from the high-temperature paramagnetic tetragonal phase to a paramagnetic orthorhombic phase at  $T_s$ , followed by a discontinuous further orthorhombic structural distortion and weakly first-order AF phase transition at  $T_N$  ( $T_N < T_s$ ) due to magnetoelastic coupling [5]. Upon Ni doping in  $\text{BaFe}_{2-x}\text{Ni}_x\text{As}_2$ , the structural and magnetic phase transitions are gradually separated and suppressed [Fig. 1(a)], and become second order in nature [7–10]. Upon application of a uniaxial pressure, the  $C_4$  rotational symmetry of the tetragonal lattice is broken. Since the tetragonal-to-orthorhombic symmetry of the underlying lattice can only be broken once,  $T_s$  will become a crossover regardless of the magnitude of the applied pressure, as our findings in Figs. 3 and 4 corroborate. The same conclusion holds for  $\text{SrFe}_{1.97}\text{Ni}_{0.03}\text{As}_2$  where the first-order structural transition becomes a crossover [see Figs. 4(g) and 4(h)]. Therefore, both  $\text{BaFe}_{2-x}\text{Ni}_x\text{As}_2$  and  $\text{SrFe}_{1.97}\text{Ni}_{0.03}\text{As}_2$  under uniaxial pressure can only exhibit AF phase transition. We note that our measurements and theoretical Landau-Ginzburg analysis do not rely on the microscopic nature of the nematic order parameter  $\varphi$ . In particular, they apply equally well to the so-called Ising spin nematic scenario [25–29] or the orbital order interpretation of nematicity [30–36]. In fact, the ferro-orbital order  $\varphi_{\text{orb}} = \langle n_{xz} - n_{yz} \rangle$  is always linearly coupled [26,36] to the Ising spin nematic order parameter  $\varphi_{\text{spin}} = \langle \mathbf{S}_i \cdot \mathbf{S}_{i+\hat{x}} - \mathbf{S}_i \cdot \mathbf{S}_{i+\hat{y}} \rangle$ , so the orbital order is generically present whenever  $\varphi_{\text{spin}} \neq 0$ , although there are theoretical indications that the converse is not always true. In other words, the orbital order can exist in the absence of static AF order [36], as is known to be the case in FeSe [57–59]. In either case, the application of external uniaxial stress renders the nematic transition a crossover, so that the lattice distortion  $\delta$  and consequently  $\varphi$  are both finite above the zero-stress value of  $T_s$ . In this light, the electronic anisotropy seen in the magnetic torque [21] and scanning tunneling microscopy [43] measurements above  $T_s$  without explicit external uniaxial pressure is likely due to intrinsic local strain in these materials which breaks the  $C_4$  rotational symmetry of the paramagnetic tetragonal phase. Indeed, local strain-induced effect has recently been observed in free standing  $\text{BaFe}_2\text{As}_2$  above  $T_N$  and  $T_s$  [60].

The key finding of the present work is that undoped  $\text{BaFe}_2\text{As}_2$ , as well as  $\text{BaFe}_{1.97}\text{Ni}_{0.03}\text{As}_2$  and  $\text{SrFe}_{1.97}\text{Ni}_{0.03}\text{As}_2$  all exhibit similar magnitudes of the pressure-induced lattice orthorhombicity [Figs. 1(c) and 4] and FWHM of  $\Delta d/d$  near  $T_N$  (Fig. 3). This indicates that these samples experience

similar strain field under nominally similar applied uniaxial pressure, thus suggesting that the doped Ni impurities do not play an important role in determining the strain field inside the sample. Theoretically, the electronic anisotropy of the iron pnictides is expected to couple linearly to the lattice orthorhombicity  $\delta$  [26–29], as captured by the effective Landau free energy in Eq. (1). The Curie-Weiss-like temperature dependence of the uniaxial pressure induced lattice distortion [Fig. 1(c)] is consistent with the temperature dependence of the nematic susceptibility  $d\delta/dP$  in Eq. (3) and agrees with the results of Young’s modulus measurements [38]. This gives us confidence that in the effective Landau description [50], the uniaxial pressure-induced lattice distortion  $\delta$  has a component proportional to the electronic nematic order parameter  $\varphi$  via Eq. (2), where one expects  $\delta \propto \varphi$  in zero pressure ( $P = 0$ ). Since  $\delta$  has similar magnitude in  $\text{BaFe}_2\text{As}_2$ ,  $\text{BaFe}_{1.97}\text{Ni}_{0.03}\text{As}_2$ , and  $\text{SrFe}_{1.97}\text{Ni}_{0.03}\text{As}_2$  (see Fig. 4), one would also expect comparable values of  $\varphi$  in all three compounds. So if one uses the resistivity anisotropy  $\Delta\rho = (\rho_b - \rho_a)/(\rho_b + \rho_a)$  as a proxy for the nematic order parameter, as has been widely used in the literature [12,20,23,24], how does one then explain the resistivity anisotropy differences in  $\text{BaFe}_{2-x}\text{T}_x\text{As}_2$  [14] and a much smaller resistivity anisotropy above  $T_N$  [Fig. 1(b)] in  $\text{SrFe}_{2-x}\text{T}_x\text{As}_2$  family of materials [18]? The bare value of the elastic shear modulus  $C_{66,0}$  that enters Eq. (A16) has no strong temperature dependence [38] and from the Curie-Weiss fits of the nematic susceptibility to Eq. (A20), we find it to be roughly the same in all three compounds,  $C_{66,0} \approx 50$  GPa [50]. The only remaining unknown variable is the elastonematic coupling constant  $\lambda$ , which could be material dependent but not temperature dependent [20,38]. It is thus very challenging to explain the qualitatively different temperature dependence of the resistivity anisotropy in  $\text{BaFe}_{1.97}\text{Ni}_{0.03}\text{As}_2$  [monotonic, blue diamonds in Fig. 1(b)] from that in  $\text{BaFe}_2\text{As}_2$  and in  $\text{SrFe}_{1.97}\text{Ni}_{0.03}\text{As}_2$  [both nonmonotonic, with a maximum at or just below  $T_s$ ]. One possible explanation for the nonmonotonic temperature dependence of the resistivity anisotropy, recently proposed in the context of FeSe [61], is to assume a temperature-dependent coefficient of proportionality between  $\Delta\rho$  and  $\varphi$ :

$$\Delta\rho(T) = \Upsilon(T)\varphi(T), \quad (4)$$

such that  $\Upsilon(T)$  tends to zero as  $T \rightarrow 0$ , whereas  $\varphi(T)$  is expected to increase monotonically below  $T_s$  as the temperature is lowered (consider for instance the mean-field result  $\varphi(T) \propto \sqrt{T_s - T}$  for the second-order phase transition).

Even with the introduction of  $\Upsilon(T)$  in Eq. (4), which has a meaning of the temperature-dependent scattering function, it is extremely difficult to explain the much lower value of  $\Delta\rho$  in  $\text{SrFe}_{1.97}\text{Ni}_{0.03}\text{As}_2$  compared to  $\text{BaFe}_2\text{As}_2$  and  $\text{BaFe}_{1.97}\text{Ni}_{0.03}\text{As}_2$ . In fact, from the Curie-Weiss fits of the susceptibility data, we estimate the elastonematic coupling constant  $\lambda$  to be a factor of  $\sim 5$  smaller in  $\text{SrFe}_{1.97}\text{Ni}_{0.03}\text{As}_2$  compared to  $\text{BaFe}_{1.97}\text{Ni}_{0.03}\text{As}_2$  [50]. Given the comparable magnitudes of  $\delta$  between the two compounds [see Figs. 4(d) and 4(h)], one would then expect the nematic order parameter  $\varphi$  to be a factor of  $\sim 5$  greater in  $\text{SrFe}_{1.97}\text{Ni}_{0.03}\text{As}_2$ , to ensure that the left-hand side of Eq. (2) remains of the same magnitude. And yet the resistivity anisotropy  $\Delta\rho \propto \varphi$

presents a diametrically opposite picture, being much smaller in  $\text{SrFe}_{1.97}\text{Ni}_{0.03}\text{As}_2$ .

We propose that a likely resolution of this dilemma lies in the nature of the magnetic phase transition which we have so far neglected in our analysis. Indeed, it is well established that structural and magnetic phase transitions in  $\text{SrFe}_{2-x}\text{T}_x\text{As}_2$  are coupled first-order transitions that decrease with increasing  $x$  before vanishing near optimal superconductivity [11], while electron-doped  $\text{BaFe}_2\text{As}_2$  has second-order magnetic and structural phase transitions [7–10]. Although application of a uniaxial pressure renders the structural transition a crossover, the first-order nature of the magnetic transition means a vanishing critical regime with suppressed low-energy spin fluctuations at temperatures near  $T_N$ , compared with those of  $\text{BaFe}_{2-x}\text{T}_x\text{As}_2$  where the AF phase transition is second order. One expects the scattering of electrons on the magnetic fluctuations, and hence the resistivity, to therefore be smaller in the vicinity of the first-order magnetic transition, as is the case in  $\text{SrFe}_{2-x}\text{T}_x\text{As}_2$ . We thus conclude that the vanishing resistivity anisotropy above  $T_N$  in the uniaxial pressure detwinned  $\text{SrFe}_{2-x}\text{T}_x\text{As}_2$  (compared with those of  $\text{BaFe}_{2-x}\text{T}_x\text{As}_2$ ) is likely rooted in the first-order nature of the AF phase transition. This is also consistent with the increased paramagnetic resistivity anisotropy on moving from  $\text{BaFe}_2\text{As}_2$  to  $\text{BaFe}_{1.96}\text{Co}_{0.04}\text{As}_2$  [15], where the magnetic transition changes from weakly first order to second order [5,7,8]. Similarly, the lack of large resistivity anisotropy in the paramagnetic state of uniaxial pressured  $\text{Ba}_{1-x}\text{K}_x\text{Fe}_2\text{As}_2$  [62],  $\text{Ba}_{1-x}\text{Na}_x\text{Fe}_2\text{As}_2$  [63], and  $\text{Ca}_{1-x}\text{La}_x\text{Fe}_2\text{As}_2$  [64] is likely due to the first-order nature of the paramagnetic to AF phase transition in these materials. The phenomenological Landau theory can be extended to include the coupling between nematicity  $\varphi$  and the magnetic order parameter [38,50], and our theoretical analysis shows [50] that the resulting uniaxial pressure-induced lattice distortion  $\delta(P) - \delta(0)$  reproduces semiquantitatively the experimental findings in Fig. 1(c).

We conclude that the in-plane resistivity anisotropy found in the paramagnetic state of iron pnictides depends sensitively on the nature of the magnetic phase transition and a strong elastonematic coupling between the uniaxial pressure induced lattice distortion and the electronic nematic susceptibility. We caution that while the resistivity anisotropy  $\Delta\rho$  and its dependence on the shear strain can be successfully used to extract the quantity proportional to the nematic susceptibility [20], care should be taken when equating  $\Delta\rho$  with the nematic order parameter itself. In particular, the nonmonotonic temperature dependence of  $\Delta\rho$  and its sensitivity to the nature of the magnetic phase transition remain relatively little explored and deserve further experimental and theoretical studies.

## ACKNOWLEDGMENTS

We thank A. E. Böhrer, J. H. Chu, J. Hu, and Q. Si for helpful discussions. The neutron-scattering work at Rice was supported by the US NSF-DMR-1308603, NSF-DMR-1362219, and DMR-1436006 (P.D.). A.H.N. was supported by US NSF CAREER Award No. DMR-1350237. This work is also supported by the Robert A. Welch Foundation Grants No. C-1839 (P.D.) and No. C-1818 (A.H.N.). The work at

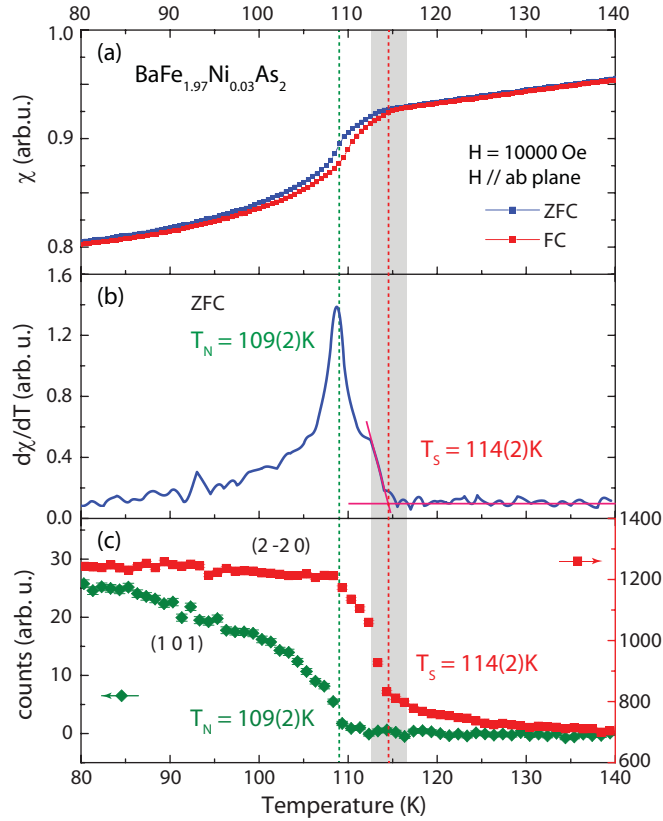


FIG. 5. (a) Temperature dependence of the magnetic susceptibility under ZFC and FC cases for  $\text{BaFe}_{1.97}\text{Ni}_{0.03}\text{As}_2$ . (b) Temperature derivative of the magnetic susceptibility, showing clearly the structural and magnetic phase transitions. (c) Temperature dependence of the  $\mathbf{Q} = (1,0,1)$  magnetic (green diamonds) and  $(2,-2,0)$  nuclear (red squares) Bragg peak intensity [41]. The extinction release of the  $(2,-2,0)$  Bragg reflection is sensitive to the change of structural distortion and used to determine the  $T_s$ . Combining the results in (a)–(c), the  $T_N$  and  $T_s$  are determined as shown in the green and red vertical dashed lines, respectively.

the Institute of Physics, Chinese Academy of Sciences, was supported by Ministry of Science and Technology of China (973 Projects No. 2012CB821400 and No. 2011CBA00110), National Natural Science Foundation of China Projects No. 11374011 and No. 91221303, and The Strategic Priority Research Program (B) of the Chinese Academy of Sciences Grant No. XDB07020300. T.K. thanks for support by the Deutsche Forschungsgemeinschaft through SFB/TRR80.

## APPENDIX

### 1. Sample Information

The iron pnictide single crystals used in the present study were prepared by the self-flux method [53]. The samples have been characterized by resistivity, magnetization, and neutron-scattering measurements. Figures 5 and 6 show the basic characterizations of  $\text{BaFe}_{1.97}\text{Ni}_{0.03}\text{As}_2$  and  $\text{SrFe}_{1.97}\text{Ni}_{0.03}\text{As}_2$  samples, respectively. The basic characteristics of the  $\text{BaFe}_2\text{As}_2$  and  $\text{BaFe}_{1.88}\text{Ni}_{0.12}\text{As}_2$  samples can be found elsewhere [41,53].

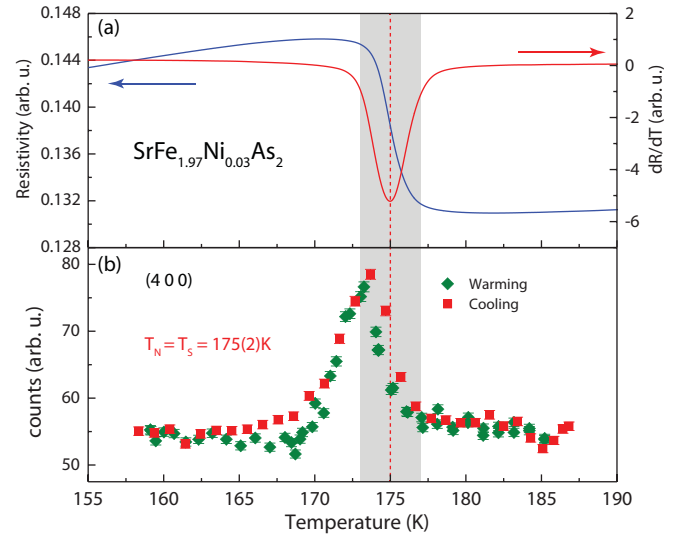


FIG. 6. (a) Temperature dependent resistivity and its temperature derivative for  $\text{SrFe}_{1.97}\text{Ni}_{0.03}\text{As}_2$ . (b) Temperature dependence of the  $(4,0,0)$  nuclear Bragg peak intensity measured for warming and cooling. The dramatic increase of the  $(4,0,0)$  Bragg reflection signals the change of structural distortion near  $T_s$  [41].

Figure 5(a) shows temperature dependence of the zero-field-cooled (ZFC) and field-cooled (FC) magnetic susceptibility  $\chi$ . Figure 5(b) is temperature derivative of  $\chi$ ,  $d\chi/dT$ . Figure 5(c) shows temperature dependence of the magnetic  $(1,0,1)$  Bragg peak (green diamonds) and  $(2,-2,0)$  nuclear Bragg intensity (red squares). These results establish  $T_N$  (green dashed line) and  $T_s$  (red dashed line) of  $\text{BaFe}_{1.97}\text{Ni}_{0.03}\text{As}_2$ . The  $T_N$  was determined as  $109 \pm 2$  K from magnetic order parameter of the  $(1,0,1)$  magnetic Bragg peak [Fig. 5(c)] and temperature-dependent magnetization measurements [Fig. 5(a)]. The structural transition temperature  $T_s$  is estimated from a feature shown in the magnetization, [Fig. 5(b)], and the neutron extinction release of the  $(2,-2,0)$  nuclear Bragg peak intensity [Fig. 5(c)] [41,65,66].

Figure 6(a) shows temperature-dependent resistivity  $R$  and its derivative  $dR/dT$  for  $\text{SrFe}_{1.97}\text{Ni}_{0.03}\text{As}_2$ . The dip of the  $dR/dT$  at  $T = 175$  K indicates the concomitant structural and magnetic transition, different from the two features for the separated  $T_N$  and  $T_s$  in  $\text{BaFe}_{1.97}\text{Ni}_{0.03}\text{As}_2$ . Figure 6(b) is temperature dependence of the  $(4,0,0)$  nuclear Bragg peak intensity. The dramatic increase of the peak intensity also signals the structural transition. The observed intensity hysteresis is consistent with first-order nature of the structural and magnetic phase transition.

Large single crystals were selected and cut into rectangular shapes along the orthorhombic  $[1,0,0]$  and  $[0,1,0]$  directions by a high precession wire saw. The well-cut samples were placed inside a uniaxial pressure device with  $b$  axis being the direction of the applied pressure [41]. The applied uniaxial pressures for the samples range from  $P \approx 10$  MPa to  $P \approx 20$  MPa, as described before.

In order to measure temperature and pressure dependence of orthorhombic lattice distortion  $\delta = (a - b)/(a + b)$ , the samples were mounted in the  $[H, K, 0]$  scattering plane, where orthorhombic  $(4,0,0)$  and  $(0,4,0)$  Bragg reflections can be

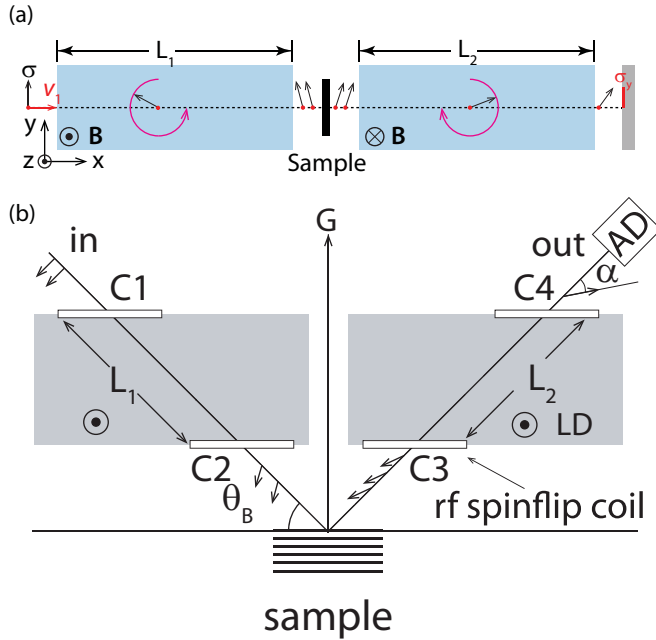


FIG. 7. (a) Basic principles for neutron spin echo with schematics of the experimental setup. The magnetic guide field  $\mathbf{B}$  directions are clearly marked. (b) Schematic diagram for the neutron Larmor diffraction measurements. For NRSE, the neutron precession direction in  $L_1$  is opposite to that of  $L_2$ . In neutron Larmor diffraction, the neutron precession directions are same in  $L_1$  and  $L_2$ .

measured. The effects of uniaxial pressure on tetragonal-to-orthorhombic structural transition and uniaxial pressure induced lattice orthorhombicity can be probed directly via measuring temperature and pressure dependence of the  $(4,0,0)$  and  $(0,4,0)$  reflections by neutron Larmor diffraction. For magnetic measurements, the  $\text{BaFe}_{1.97}\text{Ni}_{0.03}\text{As}_2$  sample was mounted in the  $[1, 1, 2] \times [1, -1, 0]$  scattering plane, where both the  $(1,0,1)$  and  $(0,1,1)$  magnetic Bragg peaks can be reached [41].

## 2. Neutron resonance spin-echo measurements

Neutron spin-echo (NSE) technique has been demonstrated to be an effective method to measure the slow dynamics (quasielastic scattering) with an extremely high-energy resolution ( $\sim 1 \mu\text{eV}$  or even to  $\sim 1 \text{neV}$ ) [46]. By combining triple axis spectrometer and neutron resonance spin-echo (NRSE) techniques, the TRISP spectrometer at the Forschungsneutronenquelle Heinz Maier-Leibnitz (MLZ) is capable of measuring the lifetime of excitations with an energy resolution  $\Delta E \sim 1 \mu\text{eV}$  in the range of about 1–200  $\mu\text{eV}$  [67].

Compared with typical neutron-scattering experiments where  $S(\mathbf{Q}, \omega)$  ( $E = \hbar\omega$ ) is usually measured, neutron spin-echo measures  $I(\mathbf{Q}, \tau_{\text{NSE}})$  or  $P(\mathbf{Q}, \tau_{\text{NSE}})$ , where  $P$  is the polarization of the scattered neutrons, which is the time Fourier transform of the  $S(\mathbf{Q}, \omega)$  and thus provides direct information of  $S(\mathbf{Q}, \omega)$  such as energy linewidth (lifetime) and intensity [48,68].

The basic principle of NSE can be understood in a simplified picture as shown in Fig. 7(a). We assume neutrons polarized along the  $y$  direction with a velocity  $v_1$  enter the first

arm of NSE spectrometer with a constant magnetic field  $\mathbf{B}$  [Fig. 7(a)]. The precession angle in the first arm ( $L_1$ ) is then  $\phi_1 = \omega_L t = \gamma |\mathbf{B}| L_1 / v_1$ , where  $\gamma = 2\mu_N / \hbar = 2.916 \text{ kHz/G}$  is the gyromagnetic ratio of neutron,  $L_1$  is the length of the first neutron guide arm, and  $t$  is the time for neutron to travel through the first arm. After interactions with the sample, some neutrons are scattered into different energy with velocity  $v_2$ . In the second arm ( $L_2$ ), the neutron spin will precess along the opposite direction, generating  $-\phi_2 = -\omega_L L_2 / v_2$ . Assuming  $L_1 = L_2 = L$  and  $v_2 = v_1 + \delta v$ ,  $\delta v \ll v_1$ , the net phase after passing through both field regions will be  $\phi = \frac{\omega_L L}{v_1} \delta v$ . Since neutron energy transfer is  $\hbar\omega = \frac{1}{2}m(v_2^2 - v_1^2) \approx mv_1 \delta v$ , the net phase can be written as

$$\phi = \left( \frac{\hbar\omega_L L}{mv_1^3} \right) \omega \equiv \omega \tau_{\text{NSE}}, \quad (\text{A1})$$

where  $\tau_{\text{NSE}}$  is defined as

$$\tau_{\text{NSE}} = \left( \frac{\hbar\omega_L L}{mv_1^3} \right) = 1.863 \times 10^{-16} B(\text{G})L(\text{cm})\lambda^3(\text{\AA}) \quad (\text{A2})$$

Note  $\tau_{\text{NSE}}$  is not a physical time but a quantity determined by specific parameters of the spectrometer, with the dimension of time.

The polarization along  $y$  direction of the scattered neutrons can be analyzed and detected [Fig. 7(a)]. The average polarization  $\langle \sigma_y \rangle$  for neutrons with energy transfer  $\hbar\omega$  is

$$\langle \sigma_y \rangle = \langle \cos\phi \rangle = \int d\omega S(\mathbf{Q}, \omega) \cos\omega \tau_{\text{NSE}}. \quad (\text{A3})$$

Thus  $\langle \sigma_y \rangle$  is the cosine Fourier transform of  $S(\mathbf{Q}, \omega)$  for  $\omega$  and has been shown equal to the intermediate scattering function  $I(\mathbf{Q}, \tau)$ . Therefore, the  $\tau_{\text{NSE}}$  dependent polarization  $P(\tau)$ , that is,  $I(\mathbf{Q}, \tau)$ , provide direct information about  $S(\mathbf{Q}, \omega)$  [48].

In the NRSE, the precession fields and spin flippers are replaced by four short bootstrap rf spin flipper coils [C1–C4 in Fig. 7(b)], which can improve the energy resolution by a factor of 4 compared with the NSE with the same  $\mathbf{B}$  and  $L$ . The neutrons only precess in bootstrap while keep their spin directions in  $L_1$  and  $L_2$ .  $L_2$  can be tuned by translating the flipper C4, by which the intensity with respect to the position of C4,  $I(x_{c4})$ , can be measured. For a fixed  $\tau$ , the measured intensity can be described as

$$I(x_{c4}) = \frac{I_0}{2} \left[ 1 + P \cos \left( \frac{2\pi}{\Delta x_{c4}} (x_{c4} - x_{c4,0}) \right) \right], \quad (\text{A4})$$

where  $P$  is the polarization,  $I_0$  is the averaged intensity of the scattered beam,  $\Delta x_{c4}$  is the period of the intensity modulation, and  $x_{c4,0}$  is the reference position of C4.

The measurements of the  $P(\tau)$  for  $\text{BaFe}_{1.97}\text{Ni}_{0.03}\text{As}_2$  under  $P \approx 15 \text{ MPa}$  are summarized in Fig. 8. Figure 8(a) shows the intensity modulations for  $\tau = 16.29$  and  $39.25 \text{ ps}$  of  $\mathbf{Q} = (1,0,1)$  at  $T = 102 \text{ K}$ . The polarizations are obtained through fitting the data by Eq. (A4). The fitted  $P(\tau)$  for different temperatures are plotted in Fig. 8(b). Assuming the possible broadening in energy of the magnetic reflections is caused by some slow dynamics (quasielastic scattering), the corresponding  $S(\omega)$  can be described by a simple Lorentzian:

$$S(\omega) = \frac{1}{\pi} \frac{\Gamma}{(\omega - \omega_0)^2 + \Gamma^2}, \quad (\text{A5})$$

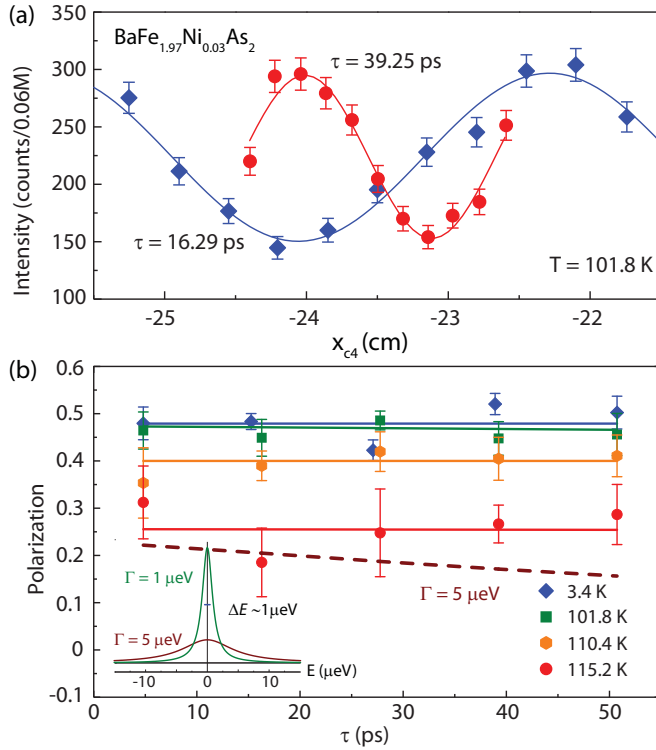


FIG. 8. (a) Measurements of the neutron polarization in one period of  $\phi$  for  $\tau = 16.29$  and  $39.25$  ps. The solid lines are cosine fittings of the data using Eq. (A4). (b)  $P(\tau)$  for various temperatures. The solid lines are fittings by Eq. (A6). The brown dashed line shows a drawing of Eq. (A6) with  $\Gamma = 5 \mu\text{eV}$  for comparison purpose. The corresponding Lorentzian  $S(\omega)$  are shown as the solid green and brown lines in the inset.

where  $\Gamma$  ( $\Gamma \geq 0$ ) (half width at half maximum) is the linewidth of the quasielastic scattering ( $\omega_0 = 0$ ). Followed by Eq. (A5), the  $P(\tau)$  should be fitted by the Fourier transform of Eq. (A5):

$$P(\tau) = P_0 \exp\left(-\frac{\Gamma\tau}{\hbar}\right). \quad (\text{A6})$$

All the  $P(\tau)$  in our measurements can be well described by this exponential decay, as shown in Fig. 8(b). The fitted energy linewidths  $\Gamma$  are less than  $1 \mu\text{eV}$ , meaning the signals are resolution limited at the measured temperatures. The comparison between  $S(\omega)$  for resolution limited ( $\Gamma \leq 1 \mu\text{eV}$ ) and  $\Gamma = 5 \mu\text{eV}$  is shown in the inset of Fig. 8(b), as a reference. The temperature dependence of  $\Gamma$  is shown in Fig. 2(b) of the main text, which must have values greater than zero. The large error bars for the values of  $\Gamma$  near  $T_N$  are due to experimental uncertainties of  $P(\tau)$  in Fig. 8(b).

### 3. Larmor diffraction measurements

We now turn to the neutron Larmor diffraction measurements. Larmor diffraction is a neutron Larmor precession technique capable of measuring lattice spacing expansion and spread with a resolution better than  $10^{-5}$  in terms of  $\Delta d/d$ . It is sensitive to minor change of lattice spacing  $d$  but insensitive to sample mosaicity and not much affected by slight misalignment [69]. The total precession phase ( $\phi_{\text{tot}}$ )

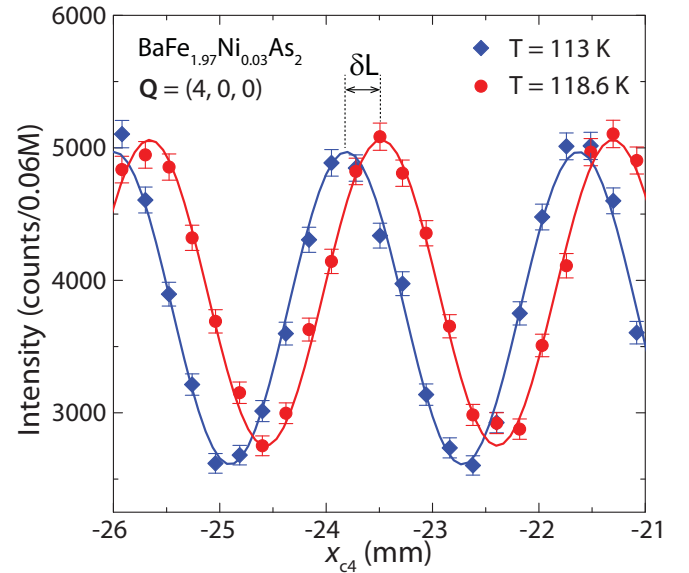


FIG. 9. Measurement of the  $\Delta\phi_{\text{tot}}$  between  $T = 113$  K and  $T = 118.6$  K, by which the relative change of  $d$  spacing can be tracked.

dependent polarizations [ $P(\phi_{\text{tot}})$ ] can be used to determine the  $d$  spread and the splitting between multiple  $d$  spacings with small differences, such as the peak splitting caused by the tetragonal-to-orthorhombic structural transitions in iron pnictides [41].

Figure 7(b) is a schematic of Larmor diffraction. The spin flippers are tuned to be parallel with the diffracting planes and the neutron precession directions in  $L_1$  and  $L_2$  are the same. Assuming  $L_1 = L_2 = L$ , the total neutron precession phase is  $\phi_{\text{tot}} = 2\omega_L L/v$ . From the Bragg law  $|\mathbf{Q}| = |\mathbf{G}| = 2k_i \sin \theta_B$ ,  $|\mathbf{G}| = 2\pi/d$ , and the neutron velocity  $v = \hbar k_i/m$ , the total Larmor phase  $\phi_{\text{tot}}$  can be written as

$$\phi_{\text{tot}} = \frac{2\omega_L L m \sin \theta_B}{\pi \hbar} d. \quad (\text{A7})$$

Consequently, the variation of the Larmor phase is proportional to the change of the  $d$  spacing (caused by external or thermal effect), that is

$$\Delta\phi_{\text{tot}} = \phi_{\text{tot}} \frac{\Delta d}{d}. \quad (\text{A8})$$

For  $d$  change induced thermal expansion, the evolution of  $P(\phi_{\text{tot}})$  at different temperatures and the relative change of the  $\phi_{\text{tot}}$  ( $\Delta\phi_{\text{tot}}$ ) can be obtained by fitting the intensity modulations  $I(\phi_{\text{tot},0} + \Delta\phi)$  using Eq. (A4), where the modulations are measured by scanning  $x_{c4}$  near  $x_{c4,0}$  [Figs. 7(b) and 9]. The  $\Delta\phi_{\text{tot}}$  between different temperatures (or pressures/ $\mathbf{Q}$ s) can be used to determine the evolution of the lattice spacings. To facilitate data analysis,  $\Delta\phi_{\text{tot}}$  between two neighboring conditions should be kept within  $2\pi$ . Figure 9 is an example of lattice thermal expansion at  $\mathbf{Q} = (4,0,0)$  of  $\text{BaFe}_{1.97}\text{Ni}_{0.03}\text{As}_2$ . The difference in  $x_{c4}$  ( $\delta L$ ) between  $T = 113$  and  $118.6$  K,  $\delta L$ , can be converted to lattice expansions according to Eqs. (A7) and (A8). In present measurements, 1 mm is equivalent to  $\sim 1 \times 10^{-3}$  in  $\Delta d/d$ , with resolution  $\sim 1 \times 10^{-5}$ . Note lattice expansion measurements are only valid for single  $d$  spacing at one  $\mathbf{Q}$ . Systems showing coexisting multiple  $d$  spacings

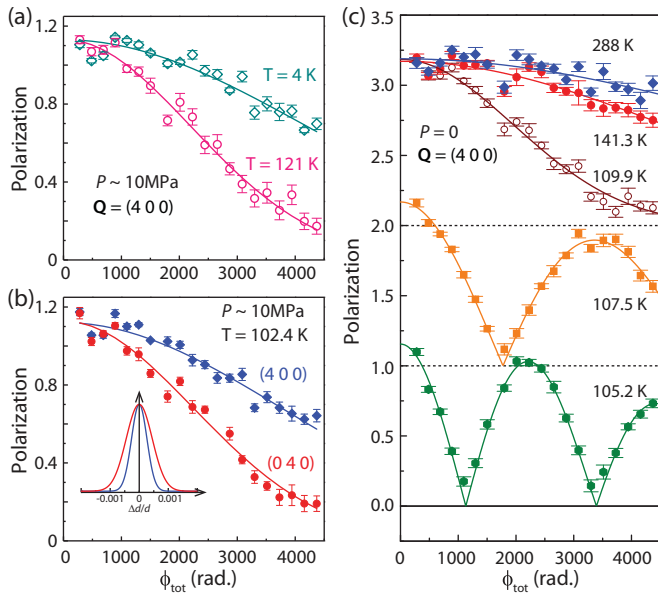


FIG. 10. Larmor diffraction measurements of  $P(\tau)$  for  $\text{BaFe}_{1.97}\text{Ni}_{0.03}\text{As}_2$ . (a) Comparison of  $P(\phi_{\text{tot}})$  at  $\mathbf{Q} = (4,0,0)$  between  $T = 4$  K and 121 K with  $P \approx 10$  MPa. (b)  $P(\phi_{\text{tot}})$  for the  $(4,0,0)$  and  $(0,4,0)$  reflections measured at  $T = 102.4$  K with  $P \approx 10$  MPa. The inset shows the Gaussian distribution of the  $d$  spacing. (c) Temperature dependence of the  $P(\phi_{\text{tot}})$  for the  $(4,0,0)$  peak at  $P = 0$ .  $P(\phi_{\text{tot}})$  for the two  $d$  spacings shows clear modulation which can be fitted by Eq. (A10) (solid curves) due to the twinning caused by the tetragonal-to-orthorhombic structural transition.

around the same  $\mathbf{Q}$  with small differences between them cannot be measured by this method.

Besides the lattice expansion measurements, the  $P(\phi_{\text{tot}}) = \langle \cos \Delta \phi(\phi_{\text{tot}}) \rangle$  in a wide range of  $\phi_{\text{tot}}$  has been demonstrated to be the Fourier transform of the lattice spacing distribution [ $f(\Delta d/d)$ ] [47,69]. For a single-Gaussian distribution of  $d$  with  $\text{FWHM} = \varepsilon_{FW}$ , the  $P(\phi_{\text{tot}})$  can be derived as

$$P(\phi_{\text{tot}}) = P_0 \exp\left(-\frac{\phi_{\text{tot}}^2 \varepsilon_{FW}^2}{16 \ln 2}\right), \quad (\text{A9})$$

where the FWHM represents the magnitude of the  $d$  spread. It is usually expressed in terms of  $\Delta d/d$ . The data shown in Fig. 3 of the main text are temperature dependence of the FWHM (lattice spacing spread). All of our  $P(\phi_{\text{tot}})$  for single  $d$  spacing are well described by this model, resulting in a Gaussian distribution of the  $d$  values. Figure 10 shows the  $P(\phi_{\text{tot}})$  of  $\text{BaFe}_{1.97}\text{Ni}_{0.03}\text{As}_2$  under  $P \approx 10$  MPa and their fittings by Eqs. (A9) and (A10). A clear difference between  $T = 4$  K and  $T = 121$  K in Fig. 10(a) indicates different FWHM of the  $d$  spread. Figure 10(b) compares  $P(\phi_{\text{tot}})$  for the  $(4,0,0)$  and  $(0,4,0)$  reflections at  $T = 102.4$  K. The corresponding FWHMs of the  $d$  distributions are also shown as an inset. Their differences suggest that the  $d$  spread along the pressure-applied orientation is much larger.

Figure 10(c) shows temperature dependence of  $P(\phi_{\text{tot}})$  for an unpressured  $\text{BaFe}_{1.97}\text{Ni}_{0.03}\text{As}_2$  sample. Its evolution at high temperature ( $T > 109$  K) indicates the broadening of the  $d$  spread. Below 109 K, clear modulations are seen in  $P(\phi_{\text{tot}})$ . This is caused by the peak splitting of the orthorhombic  $(4,0,0)$

and  $(0,4,0)$  reflections in a twinned sample. For systems showing two or more coexisting  $d$  spacings around some  $\mathbf{Q}$ , their  $d$  spacing distribution functions are superposition of multiple Gaussian distributions. In this case, the interference between different  $d$  spacings will appear and can be used to identify the specific values and spread of the involved  $d$  spacings.

For the peak splitting (two  $d$  spacings) in  $\text{BaFe}_{1.97}\text{Ni}_{0.03}\text{As}_2$ , interference between scattered neutrons from  $d_1$  and  $d_2$  gives rise to the modulating polarization

$$P(\phi_{\text{tot}}) = A \sqrt{a^2 + (1-a)^2 + 2a(1-a)\cos(\phi_{\text{tot}}\Delta\varepsilon)}, \quad (\text{A10})$$

where

$$A = P_0 \exp\left(-\frac{\phi_{\text{tot}}^2 \varepsilon_{FW}^2}{16 \ln 2}\right); \quad (\text{A11})$$

here we assume both  $d$  spacings have the same  $\varepsilon_{FW}$ .  $a$  and  $(1-a)$  denote the populations of the  $d_1$  and  $d_2$ ;

$$\Delta\varepsilon = \frac{d_1 - d_2}{(d_1 + d_2)/2} \quad (\text{A12})$$

is the lattice distortion. The definition of  $\Delta\varepsilon$  is similar to the orthorhombic lattice distortion  $\delta = (a-b)/(a+b)$  in iron pnictides, with  $\Delta\varepsilon = 2\delta$  [5]. The  $P(\phi_{\text{tot}})$  at  $T = 107.5$  and 105.2 K in Fig. 10(c) are well described by Eq. (A10). The fitted lattice distortions and  $d$  spreads are shown in Figs. 3 and 4 of the main text. The resolution in determining  $\Delta\varepsilon$  here depends on the range of  $\phi_{\text{tot}}$  and the  $d$  spread of the sample since the dips of the polarization are critical for fitting  $\Delta\varepsilon$ . The resolution of  $\Delta\varepsilon$  for two  $d$  spacings is  $7 \times 10^{-4}$  in the present work. Thus the possible distortions at temperatures slightly lower than  $T_s = 114$  K [such as the 109.5-K data shown in Fig. 10(c)] in  $\text{BaFe}_{1.97}\text{Ni}_{0.03}\text{As}_2$  cannot be distinguished from the broadening of the  $d$  spread.

Figure 11 is  $P(\phi_{\text{tot}})$  for temperatures across the structural transition of the  $\text{BaFe}_2\text{As}_2$  sample.  $P(\phi_{\text{tot}})$  in Fig. 11(a) is a beating pattern caused by interference between two  $d$  spacings below  $T_s$ , similar with that shown in Fig. 10(c). The corresponding  $d$  spacing distributions are shown in Fig. 11(e). The orthorhombic distortions can be determined as  $\delta = (d_2 - d_1)/(d_2 + d_1)$ . Upon warming the sample to  $T = 137$  K, a temperature slightly lower than  $T_s$ , a more complicated pattern [Fig. 11(b)] indicates the coexistence of four  $d$  spacings [Fig. 11(f)]. This is consistent with the coexisting orthorhombic antiferromagnetic ( $\delta_1$ ) and orthorhombic paramagnetic ( $\delta_2$ ) phases revealed by high-resolution x-ray-diffraction measurements [5]. The four- $d$  spacing model of  $P(\tau)$  can be derived analytically (not shown here) and fits the data very well. Figures 11(c) and 11(g) are results for  $T \sim T_s$ , where the  $\delta_2$  is indistinguishable and only one broad  $d$  spread can be fitted. Here, the orthorhombic antiferromagnetic phase ( $\delta_1$ ) is about to disappear, suggesting this temperature is near  $T_s$ . For temperature higher than  $T_s$  in Figs. 11(d) and 11(h), only one  $d$  spacing is observed, indicating the system enters into the paramagnetic tetragonal phase. In Figs. 11(a) and 11(b), the magnitude of the lattice distortions determines the beating periods (overall line shape) and the relative populations of different  $d$  spacings control whether the polarization can reach zero at dips. In the present study, the overall line shapes of all  $P(\tau)$  are well fitted by specific multiple (2–4)  $d$  spacing

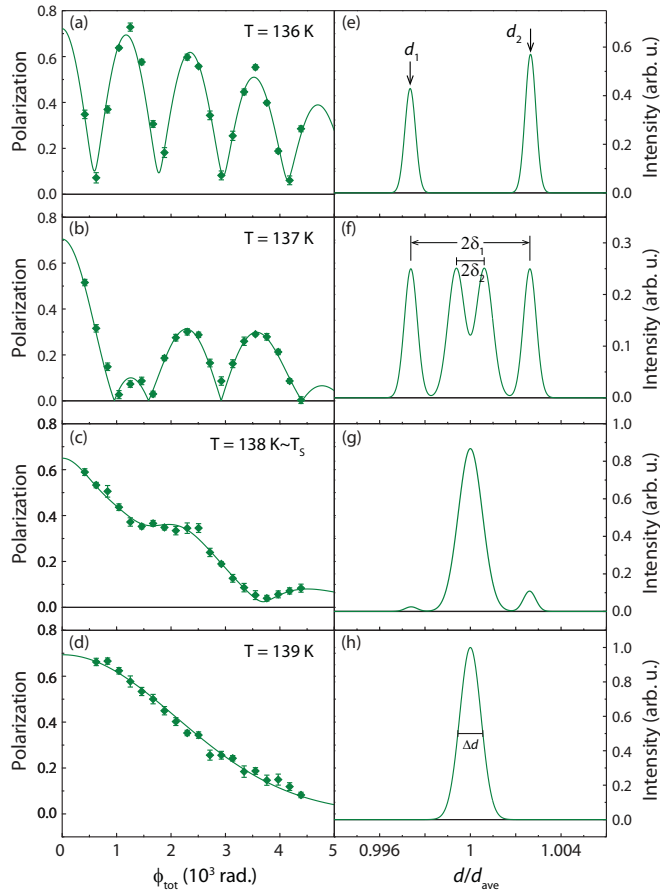


FIG. 11. (a)–(d) Precession phase ( $\phi_{\text{tot}}$ ) dependent polarizations across the structural transition for  $\text{BaFe}_2\text{As}_2$ . The solid green curves are fits of the  $P(\phi_{\text{tot}})$  by one or multi-Gaussian  $d$  spacing distribution models. (e)–(h)  $d$  spacing distributions in  $d$  space. The orthorhombic, coexisting two different orthorhombic and tetragonal phases can be determined for  $T = 136$ – $139$  K, respectively.

models [green curves in Figs. 11(a)–11(d)], indicating that the lattice distortions are well determined.

The orthorhombic lattice distortions for  $\text{BaFe}_2\text{As}_2$  and  $\text{SrFe}_{1.97}\text{Ni}_{0.03}\text{As}_2$  obtained from Larmor diffraction measurements of  $P(\phi_{\text{tot}})$  are shown in Fig. 12. These results are consistent with previous results measured by x-ray diffraction [5]. The error bars in Figs. 3 and 4 of the main text are fitting errors of the raw data at different temperatures according to formulas discussed above.

#### 4. $d$ spread anisotropy between $a$ and $b$

Our another interesting discovery is the doping dependent  $d$  spread anisotropy under uniaxial pressure. The samples shown in Fig. 13 exhibit similar temperature dependence of the  $d$  spread between (4,0,0) and (0,4,0), suggesting that the difference of  $d$  spread between  $a$  and  $b$  is trivial. However, we note that the FWHM of (0,4,0), along the uniaxial pressure direction, is much larger than  $a$  in underdoped samples [Figs. 13(a)–13(c)]. This may be attributed to an inhomogeneous distribution of the pressure induced strain field. However, we find very small differences in  $d$  spread between (4,0,0) and (0,4,0) in the overdoped  $\text{BaFe}_{1.88}\text{Ni}_{0.12}\text{As}_2$  [Fig. 13(d)], suggesting the

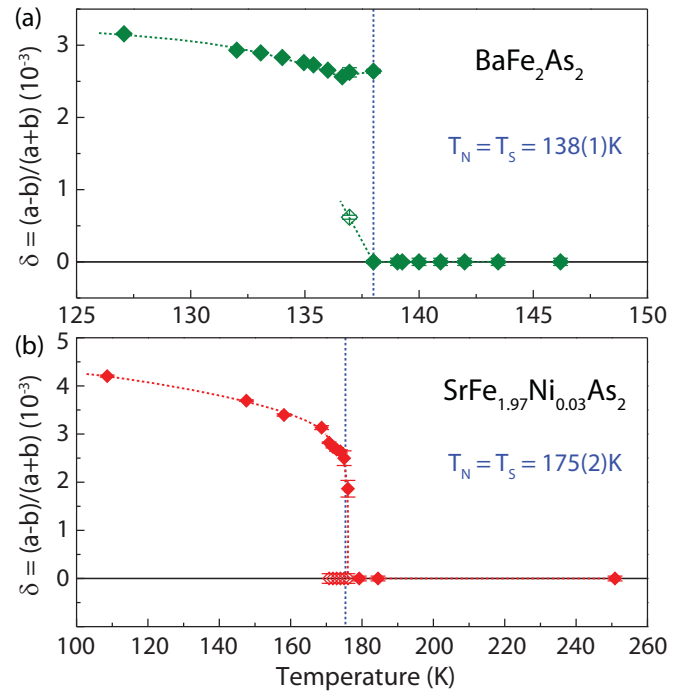


FIG. 12. Temperature-dependent orthorhombic lattice distortions for  $\text{BaFe}_2\text{As}_2$  and  $\text{SrFe}_{1.97}\text{Ni}_{0.03}\text{As}_2$ . The open green diamond in (a) marks the temperature range showing four  $d$  spacings. The open red diamonds in (b) show the persistence of the tetragonal phase into the orthorhombic phase, indicative of a first-order structural transition, consistent with previous reports. The vertical blue dashed lines mark the structural transitions.

$d$  spread anisotropy between  $a$  and  $b$  is nontrivial and may be associated with antiferromagnetic/structural instability or even nematic susceptibility in underdoped samples.

#### 5. Lattice distortions and Young's modulus

The Young's modulus  $Y$  along the  $b$  axis ( $\sim C_{66}$ ) can be estimated by  $Y = P/\delta$ , where  $\delta$  is pressure induced lattice distortion. At  $\sim 250$  K, the  $Y$  for  $\text{BaFe}_2\text{As}_2$ ,  $\text{BaFe}_{1.97}\text{Ni}_{0.03}\text{As}_2$ , and  $\text{BaFe}_{1.88}\text{Ni}_{0.12}\text{As}_2$  estimated from our neutron Larmor diffraction experiments are  $\sim 50$ ,  $\sim 50$ , and  $\sim 100$  GPa, respectively. Compared with the shear modulus  $C_{66}$  obtained by ultrasound spectroscopy [52], the estimated  $Y$  for  $x = 0$  and  $x = 0.03$  are  $\sim 30\%$  larger. These differences are mainly caused by the errors in our estimation of the applied pressure  $P$  through measuring compressed spring distances and estimated spring constant [41]. However, they will not affect temperature dependence of the pressure-induced FWHM of  $\Delta d/d$  and its comparison with other iron pnictides, and thus will not alter the conclusions of our experiments.

#### 6. Landau theory and effect of magnetism on nematicity and strain

In order to understand the distinct behavior of the observed lattice distortion in  $\text{SrFe}_{1.97}\text{Ni}_{0.03}\text{As}_2$  compared to  $\text{BaFe}_{1.97}\text{Ni}_{0.03}\text{As}_2$  [see Fig. 1(c) in the main text], we write down the Landau free energy incorporating the electronic nematic order parameter  $\varphi$ , coupled magnetoelastically to the

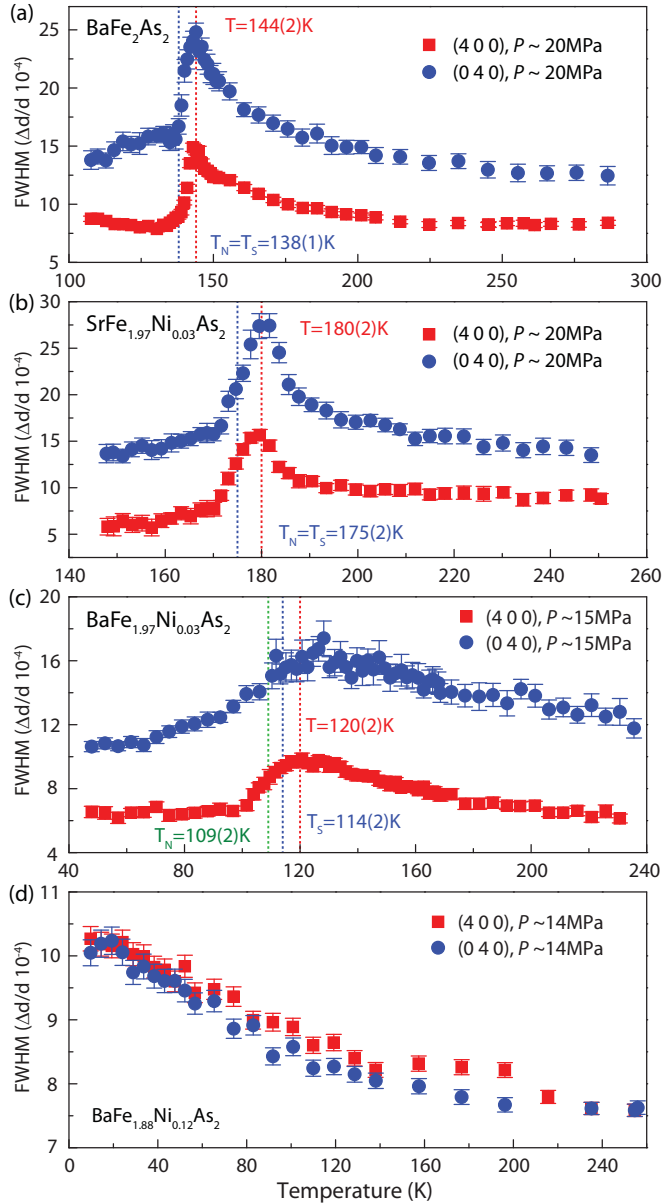


FIG. 13. Temperature and doping dependent  $d$  spread of  $\text{BaFe}_{2-x}\text{Ni}_x\text{As}_2$  and  $\text{SrFe}_{1.97}\text{Ni}_{0.03}\text{As}_2$  measured with finite uniaxial pressure.  $T_N$  and  $T_s$  are marked as blue (and green) vertical dashed lines. The red dashed line marks the temperature with the maximum of the FWHM.

lattice distortion  $\delta \propto \varepsilon_6$ , as well as to the antiferromagnetic order parameter  $M$ :

$$F = F_0 + T_0 f[\varphi, \delta] + T_0 \tilde{f}[M, \varphi], \quad (\text{A13})$$

where

$$f[\varphi, \delta] = \frac{a}{2} \frac{T - T_0}{T_0} \varphi^2 + \frac{B}{4T_0} \varphi^4 + \frac{C_{66,0}}{2T_0} \delta^2 - \frac{\lambda}{T_0} \delta \varphi - \frac{P\delta}{T_0}. \quad (\text{A14})$$

Here we chose to normalize the free energy by the Curie-Weiss temperature  $T_0$  associated with the quadratic  $\varphi^2$  term (if  $T_0$  is negative, it is replaced by  $|T_0|$ ). Treating the electronic nematic order parameter  $\varphi$  as a dimensionless variable, this has an advantage that all the coefficients in the free energy are

TABLE I. Curie-Weiss fitting parameters of the pressure-induced lattice distortions in the tetragonal state; see Fig. 1(c) in the main text.

Sample	$T_s^{CW}$ (K)	$T_0$ (K)	$T_s^{CW} - T_0$ (K)
$\text{BaFe}_2\text{As}_2$	$134.9 \pm 0.3$	$51.3 \pm 8.7$	$83.5 \pm 8.7$
$\text{SrFe}_{1.97}\text{Ni}_{0.03}\text{As}_2$	$170.9 \pm 1$	$135.7 \pm 6$	$35.2 \pm 6.1$

dimensionless (here we choose, without loss of generality,  $a = B = 1$ ). The remaining Landau expansion parameters can be fixed from the experiment. Indeed, it is convenient to express the external uniaxial stress  $P$  in terms of the dimensionless stress variable  $\sigma = P/C_{66,0}$ . Then, the last three terms in Eq. (A14) can be written as follows:

$$\frac{\lambda}{|T_0|} \left[ \left( \frac{C_{66,0}}{\lambda} \right) \left( \frac{\delta^2}{2} - \delta\sigma \right) - \delta\varphi \right]. \quad (\text{A15})$$

Minimizing the free energy with respect to  $\delta$ , we find

$$\delta = \frac{\lambda}{C_{66,0}} \varphi + \sigma. \quad (\text{A16})$$

From the minimization with respect to  $\varphi$ , it is easy to obtain

$$\frac{d\varphi}{d\delta} = \frac{\lambda}{a(T - T_0) + 3B\phi^2} \quad (\text{A17})$$

and now the shear modulus  $C_{66} \equiv dP/d\delta = d^2F/d\delta^2$  becomes

$$C_{66} = C_{66,0} - \lambda \frac{d\varphi}{d\delta} = C_{66,0} - \frac{\lambda^2}{a(T - T_0) + 3B\phi^2}; \quad (\text{A18})$$

in other words the elastic modulus gets renormalized from its bare value  $C_{66,0}$  by virtue of the elastonematic coupling  $\lambda$ . Equivalently, it follows from the above equation that the inverse nematic susceptibility  $\chi_\varphi^{-1} \equiv d^2F/d\varphi^2|_{\varphi \rightarrow 0}$  also gets renormalized from its bare value  $\chi_\phi^{-1} = a(T - T_0)$ :

$$\tilde{\chi}_\varphi^{-1} = \chi_\phi^{-1} - \frac{\lambda^2}{C_{66,0}} = a(T - T_s^{CW}), \quad (\text{A19})$$

where  $T_s^{CW} = T_0 + \frac{\lambda^2}{aC_{66,0}}$  is the renormalized Curie-Weiss temperature. One can now cast Eq. (A18) above the transition temperature  $T_s = T_s^{CW}$  into the form

$$\frac{d\delta}{dP} \equiv \frac{1}{C_{66}} = \frac{1}{C_{66,0}} \frac{T - T_0}{T - T_s^{CW}}, \quad (T > T_s^{CW}), \quad (\text{A20})$$

which is Eq. (3) in the main text. We now use this Eq. (A20) to fit the data for the pressure-induced distortion  $\delta(P) - \delta(0) \approx P(d\delta/dP)$  [Fig. 1(c) in the main text], extracting the values of  $T_0$  and  $T_s^{CW}$  which we quote in Table I for  $\text{BaFe}_2\text{As}_2$  and  $\text{SrFe}_{1.97}\text{Ni}_{0.03}\text{As}_2$ .

We now turn to the question of the strength of the elastonematic coupling constant  $\lambda$ . The unknown dimensionless parameter  $r = C_{66,0}/\lambda$  in Eq. (A16) can be fixed from the ratio  $\varphi/\delta$  in zero external stress ( $\sigma = 0$ ). Substituting the typical value of  $\delta \sim 3 \times 10^{-3}$  in  $\text{SrFe}_{1.97}\text{Ni}_{0.03}\text{As}_2$  and  $\text{BaFe}_{1.97}\text{Ni}_{0.03}\text{As}_2$  and choosing the value of the nematic order parameter  $\varphi = 1$  deep inside the nematic phase for convenience, we find  $r \sim 300$ . As for the value of  $\tilde{\lambda} = \lambda/|T_0|$  itself, it can also be fixed from the experiment since  $\lambda$  enters

in Eq. (A19) to renormalize the Curie-Weiss temperature. Therefore, one obtains  $\tilde{\lambda} = a \frac{(T_s^{CW} - T_0)}{|T_0|} r$ . Plugging in the values of  $T_s^{CW}$  and  $T_0$  from our fittings of the lattice distortions (Table I), we obtain  $\tilde{\lambda} \approx 80$  for  $\text{SrFe}_{1.97}\text{Ni}_{0.03}\text{As}_2$  and  $\tilde{\lambda} \approx 490$  for  $\text{BaFe}_2\text{As}_2$ , in other words the effective electron-lattice coupling is about  $\sim 6$  times weaker in  $\text{SrFe}_{1.97}\text{Ni}_{0.03}\text{As}_2$  compared to the  $\text{BaFe}_{2-x}\text{T}_x\text{As}_2$  compounds. For  $\text{BaFe}_{1.97}\text{Ni}_{0.03}\text{As}_2$ , the quality of our data was insufficient to accurately determine the bare Curie-Weiss temperature  $T_0$  (we were only able to determine  $T_s^{CW} = 88.5 \pm 1.0$  K). However, from the estimated  $T_s^{CW} - T_0 \approx 50$  K by the elastic measurements [38], we can deduce the approximate value of the coupling constant  $\tilde{\lambda} \approx 390$ , similar in magnitude to undoped  $\text{BaFe}_2\text{As}_2$ .

We now turn our attention to the magnetonematic coupling. On symmetry grounds, nematic order parameter must couple to  $M^2$  (since magnetization breaks time-reversal symmetry, and  $\varphi$  does not). This can be shown explicitly by considering the magnetization  $\mathbf{M}_{A,B}$  on the two sublattices composed of the next-nearest-neighbor sites of the square lattice, in which case the nematic order parameter couples linearly to the product  $(\mathbf{M}_A \cdot \mathbf{M}_B)$  [25,28,36,70]. Note that this conclusion holds independently of whether the microscopic origin of nematicity is purely magnetic [25,28,70] or orbital [31–33,36,71]. The magnetic phase transition itself may be intrinsically second order, as in  $\text{BaFe}_{2-x}\text{T}_x\text{As}_2$  compounds, or first order, as in  $\text{SrFe}_{1.97}\text{Ni}_{0.03}\text{As}_2$ ,  $\text{Ba}_{1-x}(\text{K},\text{Na})_x\text{Fe}_2\text{As}_2$ , and  $\text{Ca}_{1-x}\text{La}_x\text{Fe}_2\text{As}_2$ . Below we consider both possibilities:

$$\tilde{f}_1[M, \varphi] = \frac{u}{2}(T - T_{N,0})M^2 - \frac{v}{4}M^4 + \frac{w}{6}M^6 - \mu\varphi M^2, \quad (\text{A21})$$

$$\tilde{f}_2[M, \varphi] = \frac{u}{2}(T - T_{N,0})M^2 + \frac{v}{4}M^4 - \mu\varphi M^2. \quad (\text{A22})$$

Since we are after the qualitative consequences of the magnetonematic coupling, the precise values of the Landau coefficients are not essential (we take  $u = v = w = 1$  and  $\mu = 0.1$  for concreteness).

Having introduced the Landau formalism above, we now study the effect of the applied external stress  $P$  on the behavior of the lattice distortion. The calculated temperature dependence of  $\delta(P) - \delta(0)$  is shown in Fig. 14 for the realistic strain  $P = 20$  MPa and is shown to depend crucially on the nature of the magnetic phase transition. Indeed, the only difference between the two curves is the sign in front of the quartic  $M^4$  terms in Eqs. (A21) and (A22), while all the other Landau expansion parameters are kept the same (the two curves are offset horizontally for clarity). Note that for small  $P$ ,  $\delta(P) - \delta(0) \approx (d\delta/dP)P$  is proportional to the nematic susceptibility, which is expected to diverge at  $T_s^{CW}$  according to Eq. (A20). Both curves in Fig. 14 exhibit an enhanced nematic susceptibility on approaching  $T_s^{CW}$ , as expected. The main difference is the shape of the curve on approaching the transition, which has a distinct asymmetric “ $\lambda$ ” shape in the case of the second-order magnetic transition, and resembles closely the experimentally measured  $\delta(P) - \delta(0)$  for  $\text{BaFe}_{1.97}\text{Ni}_{0.03}\text{As}_2$  in Fig. 1(c) (see main text). By contrast, the Néel transition is first order in  $\text{SrFe}_{1.97}\text{Ni}_{0.03}\text{As}_2$ , and the experimental behavior in Fig. 1(c) is close to the calculated

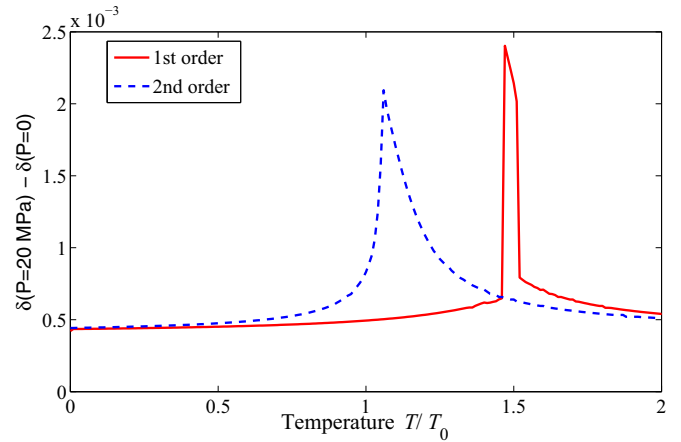


FIG. 14. Change in the lattice distortion as a function of temperature, calculated from the Landau theory assuming either first-order [Eq. (A21)] or second-order [Eq. (A22)] magnetic phase transition coupled to the nematic order parameter  $\varphi$ . The blue dashed curve is shifted to the left by  $\Delta T = 0.2T_0$  for clarity. These results should be compared to the neutron data in Fig. 1(c) in the main text.

sharp increase seen in our model (solid line in Fig. 14). Therefore, the Landau free energy results corroborate our conclusion that the nature of the magnetic transition is crucial to the observed temperature dependence of the lattice distortion.

We note in passing that for sufficiently strong coupling constant  $\mu$ , the magnetic transition becomes weakly first order even if the intrinsic free energy has a positive  $M^4$  term in Eq. (A22). This is likely the explanation for the observed change of the nature of the magnetic transition from weakly first order in  $\text{BaFe}_2\text{As}_2$  to second order upon Co doping [5,7,8]. However for the values of the coupling constants in Fig. 14, this effect is imperceptible and the main difference between the two curves is due to the different intrinsic nature of the magnetic phase transition depending on the sign of the quartic term in Eqs. (A21) and (A22). We have verified that for the significantly larger values of the coupling constant [ $\mu \gtrsim 0.4$  in Eq. (A22)], it is indeed possible to obtain the shape similar to the dashed line in Fig. 14 because the magnetic transition becomes effectively first order. In either case, our conclusions remain intact.

## 7. Interpretation of the resistivity anisotropy

The resistivity anisotropy  $\Delta\rho = (\rho_a - \rho_b)/(\rho_a + \rho_b)$  has been widely used as a proxy for the electronic nematic order parameter in the iron pnictides [12,20]. However in some compounds, in particular in  $\text{SrFe}_{1.97}\text{Ni}_{0.03}\text{As}_2$ , the resistivity anisotropy is vanishingly small immediately above  $T_N$  [see Fig. 1(b) in the main text], whereas it is much larger in  $\text{BaFe}_{2-x}\text{T}_x\text{As}_2$ . This is puzzling because the lattice distortion is comparable in both cases [Fig. 1(c)] and, according to Eq. (A16), one expects the lattice distortion  $\delta$  to be proportional to the nematic order parameter.

To shed more light on this apparent inconsistency, we have plotted in Fig. 15 the temperature dependence of the nematic order parameter  $\varphi$  under the uniaxial stress  $P = 20$  MPa. The two curves correspond to the first- and second-order

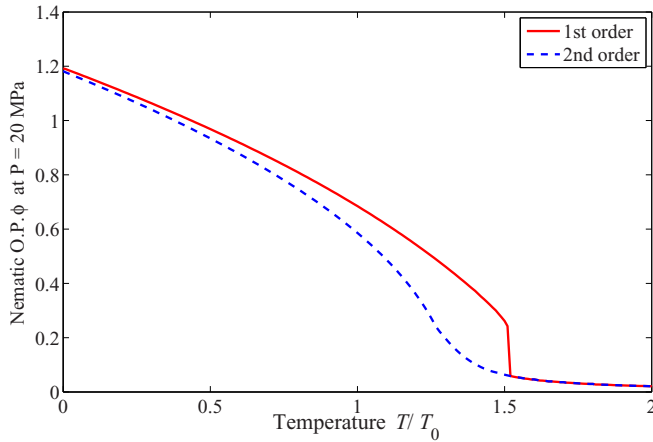


FIG. 15. Calculated temperature dependence of the nematic order parameter  $\phi$  coupled to either first- or second-order magnetic phase transition. Note that in both cases, the bare  $\phi^4$  term is positive, however the nematic transition is rendered first order (solid curve) when coupled to the first-order magnetic order parameter in Eq. (A21).

nature of the magnetic transition, respectively, and the Landau parameters were kept the same in both cases (except for the sign of the quartic term in Eqs. (A21) and (A22)). Above the transition temperature,  $T > T_s$ , the values of  $\phi$  are predictably small, but importantly, they are identical in the two cases. In fact, the main difference lies in the temperature dependence immediately below  $T_s$ . From Fig. 15, it would appear that in this regime, the nematic order parameter should be smaller for the second-order phase transition, however this is diametrically opposite from the comparison between  $\text{BaFe}_{1.97}\text{Ni}_{0.03}\text{As}_2$  and  $\text{SrFe}_2\text{As}_2$  in Fig. 1(b) (see the main text), where the magnetic transition in  $\text{BaFe}_{1.97}\text{Ni}_{0.03}\text{As}_2$  is second order, yet resistivity anisotropy is much larger. This qualitative observation can be made sharper by considering Eq. (A16), where the coupling constant  $\lambda$  is estimated from experiment to be a factor of  $\sim 5$  larger in  $\text{BaFe}_{1.97}\text{Ni}_{0.03}\text{As}_2$  and  $\text{BaFe}_2\text{As}_2$  compared to  $\text{SrFe}_{1.97}\text{Ni}_{0.03}\text{As}_2$ , whereas the elastic

modulus  $C_{66,0} \approx 50$  GPa is similar in all three materials. Then,  $\text{BaFe}_2\text{As}_2$  is expected to have at least a factor of 5 larger lattice distortion compared to  $\text{SrFe}_{1.97}\text{Ni}_{0.03}\text{As}_2$ , assuming that  $\phi$  is the same in both materials. If one now equates the resistivity anisotropy with the nematic order parameter  $\phi$ , as has commonly been done in the literature [12,20], then one is forced to conclude that  $\phi$  must be about four times larger in  $\text{BaFe}_2\text{As}_2$  due to the larger resistivity anisotropy [see Fig. 1(b)]. Taken together, one would expect the lattice distortion  $\delta$  to be a factor of  $\sim 20$  larger in  $\text{BaFe}_2\text{As}_2$  and in  $\text{BaFe}_{1.97}\text{Ni}_{0.03}\text{As}_2$  compared to  $\text{SrFe}_{1.97}\text{Ni}_{0.03}\text{As}_2$  (a factor of 4 due to larger resistivity anisotropy, times a factor of 5 due to larger  $\lambda$ ). And yet this clearly contradicts the experimental evidence in Fig. 1(c), according to which the lattice distortion is almost the same in all three materials.

One possible way out of this dilemma is that the Landau theory may not be applicable to describe the nematicity in the pnictides. However, given the excellent semiquantitative agreement that Landau theory provides for the lattice distortion (Fig. 14 above) and its well documented success describing the elastic shear modulus measurements [38], such a conclusion is perhaps not well justified. Rather, a much more plausible conclusion is that resistivity anisotropy is a poor substitute for the nematic order parameter. While it is plausible that the two quantities are proportional to each other, as follows from the nematic susceptibility measurements [20], the coefficient of proportionality need not be constant and can have a strong temperature dependence (and likely material dependence), as suggested recently by Tanatar *et al.* in the recent study on FeSe [61]. This material displays a nonmonotonic temperature dependence of the resistivity anisotropy with a peak below  $T_s$ , qualitatively similar to  $\text{BaFe}_2\text{As}_2$ . Further theoretical and experimental studies are necessary to elucidate the precise relationship of the resistivity anisotropy and the nematic order parameter in the iron pnictides and chalcogenides. Direct microscopic measurements of the nematic order parameter, for instance using the angle-resolved photoemission spectroscopy (ARPES) to probe the orbital splitting, combined with the uniaxial pressure measurements, would be desirable.

- [1] Y. Kamihara, T. Watanabe, M. Hirano, and H. Hosono, *J. Am. Chem. Soc.* **130**, 3296 (2008).
- [2] C. de la Cruz, Q. Huang, J. W. Lynn, J. Li, W. Ratcliff, II, J. L. Zarestky, H. A. Mook, G. F. Chen, J. L. Luo, N. L. Wang, and P. C. Dai, *Nature (London)* **453**, 899 (2008).
- [3] Q. Huang, Y. Qiu, Wei Bao, M. A. Green, J. W. Lynn, Y. C. Gasparovic, T. Wu, G. Wu, and X. H. Chen, *Phys. Rev. Lett.* **101**, 257003 (2008).
- [4] J. Zhao, W. Ratcliff, J. W. Lynn, G. F. Chen, J. L. Luo, N. L. Wang, J. P. Hu, and P. C. Dai, *Phys. Rev. B* **78**, 140504(R) (2008).
- [5] M. G. Kim, R. M. Fernandes, A. Kreyssig, J. W. Kim, A. Thaler, S. L. Bud'ko, P. C. Canfield, R. J. McQueeney, J. Schmalian, and A. I. Goldman, *Phys. Rev. B* **83**, 134522 (2011).
- [6] P. C. Dai, *Rev. Mod. Phys.* **87**, 855 (2015).
- [7] C. Lester, J.-H. Chu, J. G. Analytis, S. C. Capelli, A. S. Erickson, C. L. Condon, M. F. Toney, I. R. Fisher, and S. M. Hayden, *Phys. Rev. B* **79**, 144523 (2009).
- [8] S. Nandi, M. G. Kim, A. Kreyssig, R. M. Fernandes, D. K. Pratt, A. Thaler, N. Ni, S. L. Bud'ko, P. C. Canfield, J. Schmalian, R. J. McQueeney, and A. I. Goldman, *Phys. Rev. Lett.* **104**, 057006 (2010).
- [9] H. Q. Luo, R. Zhang, M. Laver, Z. Yamani, M. Wang, X. Y. Lu, M. Y. Wang, Y. C. Chen, S. L. Li, S. Chang, J. W. Lynn, and P. C. Dai, *Phys. Rev. Lett.* **108**, 247002 (2012).
- [10] X. Y. Lu, H. Gretarsson, R. Zhang, X. Liu, H. Q. Luo, W. Tian, M. Laver, Z. Yamani, Y.-J. Kim, A. H. Nevidomskyy, Q. Si, and P. C. Dai, *Phys. Rev. Lett.* **110**, 257001 (2013).
- [11] R. W. Hu, S. L. Bud'ko, W. E. Straszheim, and P. C. Canfield, *Phys. Rev. B* **83**, 094520 (2011).
- [12] J. H. Chu, J. G. Analytis, K. De Greve, P. L. McMahon, Z. Islam, Y. Yamamoto, and I. R. Fisher, *Science* **329**, 824 (2010).
- [13] M. A. Tanatar, E. C. Blomberg, A. Kreyssig, M. G. Kim, N. Ni, A. Thaler, S. L. Bud'ko, P. C. Canfield, A. I. Goldman, I. I. Mazin, and R. Prozorov, *Phys. Rev. B* **81**, 184508 (2010).

- [14] I. R. Fisher, L. Degiorgi, and Z. X. Shen, *Rep. Prog. Phys.* **74**, 124506 (2011).
- [15] S. Ishida, M. Nakajima, T. Liang, K. Kihou, C. H. Lee, A. Iyo, H. Eisaki, T. Kakeshita, Y. Tomioka, T. Ito, and S. Uchida, *Phys. Rev. Lett.* **110**, 207001 (2013).
- [16] E. C. Blomberg, M. A. Tanatar, A. Kreyssig, N. Ni, A. Thaler, R. Hu, S. L. Bud'ko, P. C. Canfield, A. I. Goldman, and R. Prozorov, *Phys. Rev. B* **83**, 134505 (2011).
- [17] E. C. Blomberg, A. Kreyssig, M. A. Tanatar, R. M. Fernandes, M. G. Kim, A. Thaler, J. Schmalian, S. L. Bud'ko, P. C. Canfield, A. I. Goldman, and R. Prozorov, *Phys. Rev. B* **85**, 144509 (2012).
- [18] S. D. Das, M. S. Laad, L. Craco, J. Gillett, V. Tripathi, and S. E. Sebastian, *Phys. Rev. B* **92**, 155112 (2015).
- [19] E. Fradkin, S. A. Kivelson, M. J. Lawler, J. P. Eisenstein, and A. P. Mackenzie, *Annu. Rev. Condens. Matter Phys.* **1**, 153 (2010).
- [20] J. H. Chu, H.-H. Kuo, J. G. Analytis, and I. R. Fisher, *Science* **337**, 710 (2012).
- [21] S. Kasahara, H. J. Shi, K. Hashimoto, S. Tonegawa, Y. Mizukami, T. Shibauchi, K. Sugimoto, T. Fukuda, T. Terashima, A. H. Nevidomskyy, and Y. Matsuda, *Nature (London)* **486**, 382 (2012).
- [22] Y. Gallais, R. M. Fernandes, I. Paul, L. Chauviere, Y.-X. Yang, M.-A. Measson, M. Cazayous, A. Sacuto, D. Colson, and A. Forget, *Phys. Rev. Lett.* **111**, 267001 (2013).
- [23] H.-H. Kuo and I. R. Fisher, *Phys. Rev. Lett.* **112**, 227001 (2014).
- [24] H.-H. Kuo, J.-H. Chu, S. A. Kivelson, and I. R. Fisher, *arXiv:1503.00402*.
- [25] R. M. Fernandes, E. Abrahams, and J. Schmalian, *Phys. Rev. Lett.* **107**, 217002 (2011).
- [26] R. M. Fernandes, A. V. Chubukov, and J. Schmalian, *Nat. Phys.* **10**, 97 (2014).
- [27] P. Chandra, P. Coleman, and A. I. Larkin, *Phys. Rev. Lett.* **64**, 88 (1990).
- [28] C. Fang, H. Yao, W.-F. Tsai, J. P. Hu, and S. A. Kivelson, *Phys. Rev. B* **77**, 224509 (2008).
- [29] J. Dai, Q. Si, J. X. Zhu, and E. Abrahams, *Proc. Natl. Acad. Sci. USA* **106**, 4118 (2009).
- [30] M. Yi, D. H. Lu, J.-H. Chu, J. G. Analytis, A. P. Sorini, A. F. Kemper, B. Moritz, S.-K. Mo, R. G. Moore, M. Hashimoto, W.-S. Lee, Z. Hussain, T. P. Devereaux, I. R. Fisher, and Z.-X. Shen, *Proc. Natl. Acad. Sci. USA* **108**, 6878 (2011).
- [31] C. C. Lee, W. G. Yin, and W. Ku, *Phys. Rev. Lett.* **103**, 267001 (2009).
- [32] F. Krüger, S. Kumar, J. Zaanen, and J. van den Brink, *Phys. Rev. B* **79**, 054504 (2009).
- [33] W. C. Lv, J. S. Wu, and P. Phillips, *Phys. Rev. B* **80**, 224506 (2009).
- [34] C.-C. Chen, J. Maciejko, A. P. Sorini, B. Moritz, R. R. P. Singh, and T. P. Devereaux, *Phys. Rev. B* **82**, 100504(R) (2010).
- [35] B. Valenzuela, E. Bascones, and M. J. Calderón, *Phys. Rev. Lett.* **105**, 207202 (2010).
- [36] Z. Wang and A. H. Nevidomskyy, *J. Phys.: Condens. Matter* **27**, 225602 (2015).
- [37] H. Kontani and Y. Yamakawa, *Phys. Rev. Lett.* **113**, 047001 (2014).
- [38] A. E. Böhmer and C. Meingast, *C. R. Phys.* **17**, 90 (2016).
- [39] C. Dhital, Z. Yamani, W. Tian, J. Zeretsky, A. S. Sefat, Z. Q. Wang, R. J. Birgeneau, and S. D. Wilson, *Phys. Rev. Lett.* **108**, 087001 (2012).
- [40] C. Dhital, T. Hogan, Z. Yamani, R. J. Birgeneau, W. Tian, M. Matsuda, A. S. Sefat, Z. Wang, and S. D. Wilson, *Phys. Rev. B* **89**, 214404 (2014).
- [41] X. Y. Lu, J. T. Park, R. Zhang, H. Q. Luo, A. N. Nevidomskyy, Q. Si, and P. C. Dai, *Science* **345**, 657 (2014).
- [42] M. P. Allan, T.-M. Chuang, F. Massee, Yang Xie, N. Ni, S. L. Bud'ko, G. S. Boebinger, Q. Wang, D. S. Dessau, P. C. Canfield, M. S. Golden, and J. C. Davis, *Nat. Phys.* **9**, 220 (2013).
- [43] E. P. Rosenthal, E. F. Andrade, C. J. Arguello, R. M. Fernandes, L. Y. Xing, X. C. Wang, C. Q. Jin, A. J. Millis, and A. N. Pasupathy, *Nat. Phys.* **10**, 225 (2014).
- [44] C. Mirri, A. Dusza, S. Bastelberger, M. Chinotti, L. Degiorgi, J.-H. Chu, H.-H. Kuo, and I. R. Fisher, *Phys. Rev. Lett.* **115**, 107001 (2015).
- [45] H. R. Man, X. Y. Lu, J. S. Chen, R. Zhang, W. L. Zhang, H. Q. Luo, J. Kulda, A. Ivanov, T. Keller, E. Morosan, Q. Si, and P. C. Dai, *Phys. Rev. B* **92**, 134521 (2015).
- [46] F. Mezei, C. Pappas, and T. Gutberlet, *Neutron Spin Echo Spectroscopy: Basics, Trends and Applications* (Springer, New York, 2003).
- [47] T. Keller, M. Th. Rekveldt, and K. Habicht, *Appl. Phys. A* **74**, s127 (2002).
- [48] S. P. Bayrakci, T. Keller, K. Habicht, and B. Keimer, *Science* **312**, 1926 (2006).
- [49] D. Hu, X. Y. Lu, W. L. Zhang, H. Q. Luo, S. L. Li, P. P. Wang, G. F. Chen, F. Han, S. R. Banjara, A. Sapkota, A. Kreyssig, A. I. Goldman, Z. Yamani, Ch. Niedermayer, M. Skoulatos, R. Georgii, T. Keller, P. S. Wang, W. Q. Yu, and P. C. Dai, *Phys. Rev. Lett.* **114**, 157002 (2015).
- [50] See the Appendix for additional data and analysis.
- [51] R. M. Fernandes, L. H. VanBebber, S. Bhattacharya, P. Chandra, V. Keppens, D. Mandrus, M. A. McGuire, B. C. Sales, A. S. Sefat, and J. Schmalian, *Phys. Rev. Lett.* **105**, 157003 (2010).
- [52] M. Yoshizawa, M. Yoshizawa, D. Kimura, T. Chiba, S. Simayi, Y. Nakanishi, K. Kihou, C.-H. Lee, A. Iyo, H. Eisaki, M. Nakajima, and S. Uchida, *J. Phys. Soc. Jpn.* **81**, 024604 (2012).
- [53] Y. C. Chen, X. Y. Lu, M. Wang, H. Q. Luo, and S. L. Li, *Supercond. Sci. Technol.* **24**, 065004 (2011).
- [54] Y. Song, S. V. Carr, X. Y. Lu, C. L. Zhang, Z. C. Sims, N. F. Luttrell, S. X. Chi, Y. Zhao, J. W. Lynn, and P. C. Dai, *Phys. Rev. B* **87**, 184511 (2013).
- [55] X. Y. Lu, D. W. Tam, C. L. Zhang, H. Q. Luo, M. Wang, R. Zhang, L. W. Harriger, T. Keller, B. Keimer, L.-P. Regnault, T. A. Maier, and P. C. Dai, *Phys. Rev. B* **90**, 024509 (2014).
- [56] F. C. Nix and D. MacNair, *Phys. Rev.* **60**, 597 (1941).
- [57] M. Bendele, A. Amato, K. Conder, M. Elender, H. Keller, H.-H. Klauss, H. Luetkens, E. Pomjakushina, A. Raselli, and R. Khasanov, *Phys. Rev. Lett.* **104**, 087003 (2010).
- [58] S. H. Baek, D. V. Efermov, J. M. Ok, J. S. Kim, J. van den Brink, and B. Büchner, *Nat. Mater.* **14**, 210 (2015).
- [59] A. E. Böhmer, T. Arai, F. Hardy, T. Hattori, T. Iye, T. Wolf, H. von Löhneysen, K. Ishida, and C. Meingast, *Phys. Rev. Lett.* **114**, 027001 (2015).
- [60] X. Ren, L. Duan, Y. W. Hu, J. R. Li, R. Zhang, H. Q. Luo, P. C. Dai, and Y. Li, *Phys. Rev. Lett.* **115**, 197002 (2015).
- [61] M. A. Tanatar, A. E. Böhmer, E. I. Timmons, M. Schütt, G. Drachuck, V. Taufour, S. L. Bud'ko, P. C. Canfield, R. M. Fernandes, and R. Prozorov, *arXiv:1511.04757*.

- [62] J. J. Ying, X. F. Wang, T. Wu, Z. J. Xiang, R. H. Liu, Y. J. Yan, A. F. Wang, M. Zhang, G. J. Ye, P. Cheng, J. P. Hu, and X. H. Chen, *Phys. Rev. Lett.* **107**, 067001 (2011).
- [63] J. Q. Ma, X. G. Luo, P. Cheng, N. Zhu, D. Y. Liu, F. Chen, J. J. Ying, A. F. Wang, X. F. Lu, B. Lei, and X. H. Chen, *Phys. Rev. B* **89**, 174512 (2014).
- [64] J. J. Ying, J. C. Liang, X. G. Luo, X. F. Wang, Y. J. Yan, M. Zhang, A. F. Wang, Z. J. Xiang, G. J. Ye, P. Cheng, and X. H. Chen, *Phys. Rev. B* **85**, 144514 (2012).
- [65] N. Ni, Ph.D. thesis, Iowa State University, 2009, p. 71.
- [66] D. K. Pratt, W. Tian, A. Kreyssig, J. L. Zarestky, S. Nandi, N. Ni, S. L. Bud'ko, P. C. Canfield, A. I. Goldman, and R. J. McQueeney, *Phys. Rev. Lett.* **103**, 087001 (2009).
- [67] T. Keller, K. Habicht, H. Klann, M. Ohl, H. Schneider, and B. Keimer, *Appl. Phys. A* **74** (Suppl.), s332 (2002).
- [68] T. Keller, R. Golub, and R. Gähler, in *Scattering: Scattering and Inverse Scattering in Pure and Applied Science*, edited by R. Pike and P. Sabatier (Academic, New York), Chap. 2.8.6.
- [69] M. Ono, Y. Waku, K. Habicht, and T. Keller, *Appl. Phys. A* **74** (Suppl.), s73 (2002).
- [70] C. Xu, M. Müller, and S. Sachdev, *Phys. Rev. B* **78**, 020501 (2008).
- [71] C.-C. Chen, B. Moritz, J. van den Brink, T. P. Devereaux, and R. R. P. Singh, *Phys. Rev. B* **80**, 180418 (2009).